Pergamon

Journal of Structural Geology, Vol. 17, No. 6, pp. 831 to 846, 1995
Elsevier Science Ltd
Printed in Great Britain
0191-8141/95 $9.50 + 0.00

0191-8141(94)00098-0

Deformation around stepovers in strike-slip fault zones

ROB WESTAWAY*

16 Neville Square, Durham DH1 3PY, U.K.

(*Received* 16 *February* 1994; *accepted in revised form* 2 *September* 1994)

Abstract— This study addresses the kinematics of stepovers in strike-slip fault zones, where left-lateral faults step rightward or right-lateral faults step leftward. A stepover is regarded as containing an internal strike-slip fault, whose ends link to transform faults, surrounded by uniformly distributed deformation. The kinematics are governed by k, the ratio of slip rates on the internal fault and transform faults, and θ, the angle between these faults. The convergence direction across the deformation, at angle Ψ to the internal fault, is an azimuth along which vectors do not rotate around vertical axes. The Lebanon stepover on the Dead Sea fault zone and the Big Bend stepover on the San Andreas fault zone provide case studies. In Lebanon, the time-averaged deformation since 15 Ma involves $k \sim 0.06$, $\theta \sim 32°$ and $\Psi \sim 34°$. It accounts for 30° of anticlockwise rotation of Cretaceous magnetization vectors in the Lebanon mountains, and ~50° rotation of Jurassic vectors. The present phase of deformation around the Big Bend, which began at ~5–7 Ma and involves $k \sim 0.89$, $\theta \sim 20°$ and $\Psi \sim 98°$, has instead only caused small rotations (both clockwise and anticlockwise). Much of this region's structure, including the dramatic (up to ~80°) clockwise rotation of magnetization vectors in the Transverse ranges, is shown to relate instead to an earlier deformation phase with much lower k.

INTRODUCTION

Many major strike-slip faults can be regarded as segmented transform faults, across which plates slip without internal deformation. They form arcs of small circles about the Euler pole around which the plates rotate, which need not be equidistant from this pole. A strike-slip fault zone may thus step sideways between segments. If the stepping is the same as the slip sense (i.e. the fault zone is right-lateral and steps rightward, or left-lateral and steps leftward), a pull-apart basin may form, which extends in the direction of slip (e.g. Mann *et al.* 1983). Where the stepping and slip are opposite (i.e. the faulting is right-lateral and steps leftward, or *vice versa*) deformation is more complex: typically including shortening and rotation around vertical axes beside strike-slip faults oriented oblique to the plate motion. Such zones have been called restraining double bends (e.g. Crowell 1974); rhomb horsts (e.g. Aydin & Nur 1982); stepovers (e.g. Aydin & Nur 1985); pressure ridges; push-up mountain ranges, blocks, or swells (e.g. Mann *et al.* 1983); knots (e.g. Muehlberger & Gordon 1987); or antidilatational jogs (e.g. Reches 1987).

Stepovers include the surroundings of Yammouneh fault in Lebanon, where the Dead Sea fault zone steps rightward, and the Big Bend region in southern California, where the San Andreas fault steps leftward. Most previous modelling has treated these regions as mosaics of rigid blocks (e.g. Carter *et al.* 1987, Ron 1987, Luyendyk 1989, Ron *et al.* 1990). However, mapping (e.g. Jennings & Strand 1969, Hancock & Atiya 1979) reveals pervasive deformation while the strike-slip faulting has been active. It thus makes no sense to assume that these regions are rigid.

Data that can constrain the kinematics of stepovers include measurements of slip rates on strike-slip faults, stress and strain orientations, and paleomagnetic observations of rotation of magnetization vectors around vertical axes. Most analyses interpret these paleomagnetic data in terms of rigid-body rotation of either large, rigid, fault-bounded blocks (e.g. Ron 1987, Luyendyk 1989), or small rigid inclusions that are either disc-shaped (e.g. Jackson 1988) or elliptical (e.g. Lamb 1987, Jackson & Molnar 1990). I assume instead that the magnetization vectors are embedded in distributed deformation, whose sense and rate are uniform spatially and over time.

OBSERVATIONS OF STEPOVERS AND THEIR INTERPRETATIONS

A stepover is regarded as containing an internal strike-slip fault with slip rate $2U$ linking transform faults with slip rates $2V$ (Fig. 1) and surrounded by distributed deformation. The ratio U/V is k; the angle between the transform faults and the internal fault is θ; and the length and width of the deformation are L and H. The strain rates for distributed simple shear and pure shear, parallel and perpendicular to the internal fault, are g and h; ζ and γ are the associated strains when these rates persist for time t. Algebraic relationships between these parameters are derived in Appendix A.

The strike of the internal fault is the natural reference direction for measuring angles in its surroundings. These include the shortening direction X_1, the initial and final orientations α_0 and α of embedded vectors, and the convergence direction Ψ between the internal fault and

*Current address: Division of Earth Sciences, Centro de Investigación Científica y de Educación, Superior de Ensenada, Apartado Postal 2732, 22860 Ensenada, Baja California, Mexico.

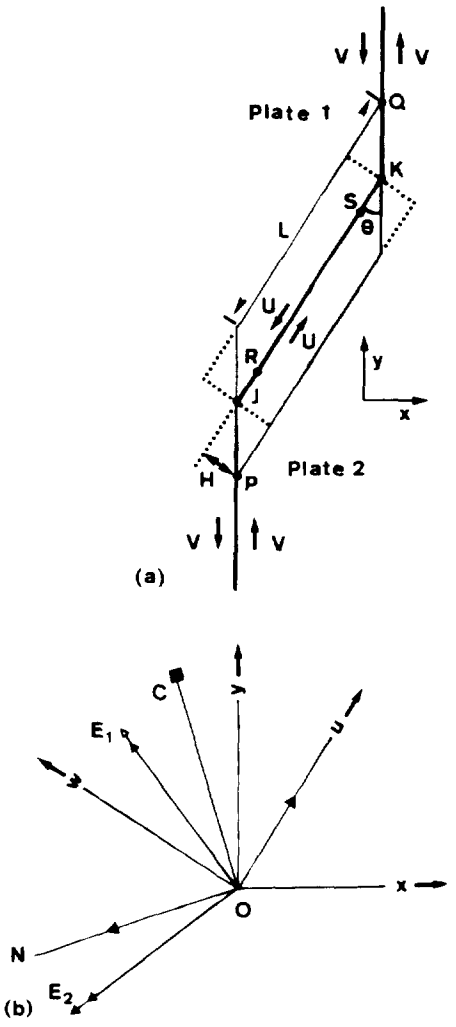

Fig. 1. (a) Assumed geometry of a rightward stepover. The left-lateral internal fault (between points J and K) slips at rate $2U$; the transform faults beyond the stepover slip at rate $2V$. The distance J–K is L; the perpendicular distance (parallel to the x-axis) between the transform fault segments is W. Both zones of distributed deformation (outlined) have width H perpendicular to the internal fault. Thin solid lines ending at points P and Q outline the actual parallelogram shape of the stepover. Dotted lines indicate the rectangular shape that is used in analysis. Points R and S are discussed in the text. (b) Coordinate systems and angular measures of deformation for Fig. 1(a). The (x,y) system has the y-axis parallel to the relative plate motion; the (u, w) system has the u-axis parallel to the internal fault. Both systems have origins at O. The angle between the u- and y-axes is θ. The principal strain rates E_1 (for shortening) and E_2 (for extension) are associated with perpendicular eigenvectors (principal axes) at azimuths X_1 and X_2 to the u-axis. The convergence direction of the surroundings to the deforming zone (the C-axis) makes angle Λ with the u-axis, this angle being identical to the azimuth Ψ along which a vector will not rotate. The directions of no length change make angles ϕ_1 and ϕ_2 with the u-axis. The first of these (ϕ_1) is always zero; the second (ϕ_2) defines the N-axis that is oblique to the u-axis and perpendicular to the C-axis. The eigenvector azimuths bisect the directions of no length change. Thus, in summary, angle u–O–N is ϕ_2, u–O–E_1 is X_1, u–O–E_2 is X_2, u–O–y is θ, u–O–C is Ψ or Λ, C–O–N is 90°, and, relative to the u-axis, ϕ_1 is zero.

the outer boundary of this deformation. Within the deformation there are two directions of no length change: the u-axis along the internal fault, and the N-axis perpendicular to the Ψ-direction. Vectors with $\alpha_0 = \Psi$ and $\alpha_0 = 0°$ do not rotate. They rotate clockwise when $0° < \alpha_0 < \Psi$, and anticlockwise when $\Psi < \alpha_0 < 180°$. Ψ is $> 90°$ for a stepover on a right-lateral fault zone and $<90°$ on a left-lateral fault zone.

This study investigates stepovers along the Dead Sea fault zone (DSFZ) in Lebanon and the San Andreas fault zone (SAFZ) in southern California. Because these localities have developed over millions of years, to assess the initial form of a stepover one must look elsewhere. The smaller Ocotillo Badlands stepover in southern California illustrates the initial form of such structures. This occupies a ~1.5 km leftward step in the right-lateral Coyote Creek fault, part of the San Jacinto fault system within the SAFZ. Local shortening (which presumably began following a recent change to the geometry of the surrounding transform faults) has uplifted Quaternary sediments, forming a ~100 m high ridge that is ~3.5 km long and ~ 1.5 km wide (e.g. Clark *et al.* 1972, Segall & Pollard 1980). This stepover does not contain any throughgoing internal strike-slip fault, so $k = 0$. However, by fitting a u-axis between its ends, θ is estimated as ~30°. Fold axes within this ridge typically trend subparallel to this axis. These folds are thus developing subparallel to the direction of no length change and no rotation within this distribution deformation.

The Dead Sea fault zone in Lebanon: observations

The N-trending Dead Sea fault zone (DSFZ) bounds the Arabian and African plates. Two of its left-lateral transform fault segments bound a ~50 km rightward step in Lebanon, which is associated with complex deformation. Many markers reveal ~105 km displacement on the southern DSFZ (e.g. Freund *et al.* 1970), which has developed since ~15 Ma at a rate of ~7 mm yr^{-1} (e.g. Westaway 1994). The main displacement constraint on the northern DSFZ is the ~70–80 km leftward offset of the ophiolite in southern Turkey (e.g. Freund *et al.* 1970). The missing ~25–35 km is either absorbed by shortening within the Arabian plate, or occurs on left-lateral faults that miss the ophiolite either offshore to the west or inland to the east. Up to ~20 km of shortening has indeed occurred within the Arabian plate east of this stepover (Chaimov *et al.* 1990). $2V$ for this stepover is thus between 7 mm yr^{-1} (105 km/15 Myr) and ~5 mm yr^{-1} (~75 km/15 Myr).

The Yammouneh fault, the internal fault within this stepover, strikes N30°E along the west-northwest margin of the Bekaa valley (Fig. 2) at ~32° to the plate motion, which is expected towards N2°W from Garfunkel's (1981) Euler pole near 33°N 23°E. Its surroundings form the Lebanon (to the west) and Anti-Lebanon mountains, which are ~20–40 km wide. The best guide to its displacement is the ~7 km length of the Yammouneh pull-apart basin (Hancock & Atiya 1970) (Fig. 2). This means k ~0.07 (7/105) to ~0.09 (7/75), time-averaged since the start of DSFZ slip. Deformation of the Lebanon mountains includes shortening perpendicular to the Yammouneh fault on folds with axes subparallel to this fault (Fig. 2). Although some localities have shortened by a factor of ~2, Hancock & Atiya

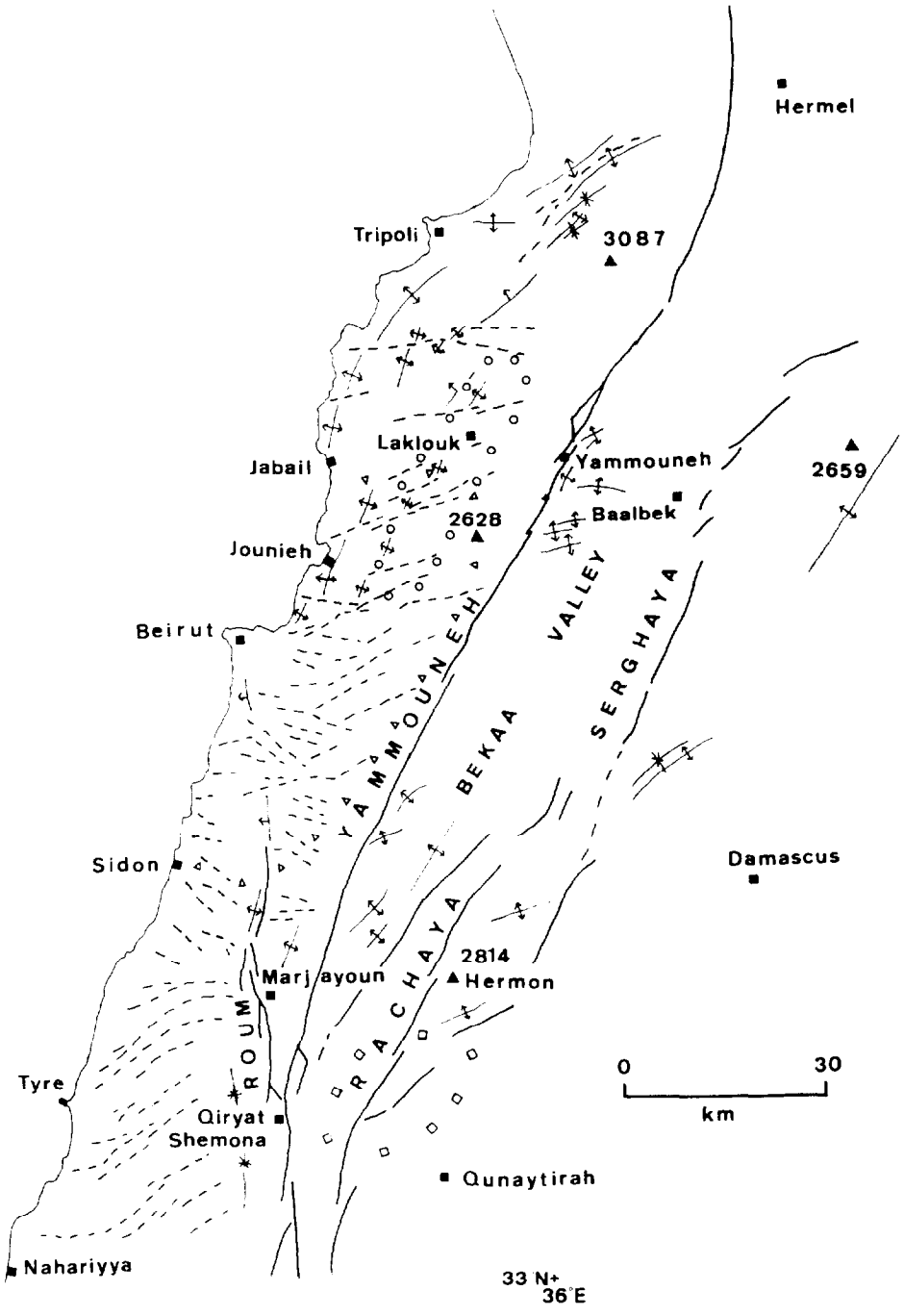

Fig. 2. Summary map of the rightward stepover to the Dead Sea fault zone in Lebanon. Thick lines denote left-lateral faults, including the Yammouneh fault. Dashed lines denote minor faults in their surrounds, most of which have small (< ~ 1 km) right-lateral offsets. Open symbols bound paleomagnetic sampling localities: circles denote zone A (Van Dongen *et al.* 1967), triangles zone B (Gregor *et al.* 1974), and squares zone C (Ron *et al.* 1990). Information is from Hancock & Atiya (1979) and Ron (1987).

(1979) considered ζ overall to be < 2. They also noted evidence of elongation subparallel to the Yammouneh fault, and secondary right-lateral faults with lengths up to ~10 km, oriented WSW–W (Fig. 2).

Studies of late Jurassic and early Cretaceous rocks reveal anticlockwise rotation of magnetization vectors in the Lebanon and Anti-Lebanon mountains. The Jurassic and Cretaceous vectors show different rotations (Table 1). If these zones comprised rigid blocks, then effects of the DSFZ would instead cause all vectors magnetized before ~15 Ma in any locality to rotate through the same angle. Cross-bedding dips in the Grès du Liban, an Early Cretaceous fluvial formation, also provide evidence for substantial anticlockwise rotation in the Lebanon mountains. These are typically westward at present, although a sediment source to the south is indicated (Gregor *et al.* 1974).

The Dead Sea fault zone in Lebanon: interpretation

The Lebanon stepover has $V = 3.0 \pm 0.5$ mm yr^{-1}. Second, with $\theta = 32°$, Ψ can be no less than 32°. Third, given their N20°W reference direction (Table 1) and the N30°E strike of the Yammouneh fault, the Early Cret-

Table 1. Paleomagnetic data from the Lebanon and Anti-Lebanon mountains

Area	Age	Ref.	N	P	D (°)	Notes
(i) Reference directions						
	K	3	28	N	160 ± 7	1
	J	4			150	2
(ii) Observations from deformed areas						
A	K	1	5	N	134 ± 6	
B	K	2	9	R	122 ± 9	
C	K	3	12	R	91 ± 13	
A	J	1	6	R	93 ± 3	
B	J	2	9	R	95 ± 11	
(iii) Past compilations of data						
B	J + K	2,3	18	R	105 ± 10	
B + C	J + K	3	30	R	99 ± 8	
(iv) Original compilations of data						
A + B	J	1,2,4	15	R	94 ± 7	3
A + B	K	1,2,4	14	R	129 ± 7	4
C	K	3,4	12	R	97 ± 13	5

Field areas A, B and C are shown in Fig. 2. Reference 1 is Van Dongen *et al.* (1974); 2 is Gregor *et al.* (1974); 3 is Ron (1987); and 4 is original results from this study. Age K is Early Cretaceous (Aptian; ~110 Ma); J is Late Jurassic (Kimmeridgian; ~150 Ma). *N* is the number of sites. Magnetic polarity *P* is N for normal or R for reversed. Declination *D* is measured clockwise from north, with 180° added for normal-polarity sites to facilitate comparison. Uncertainties in declination are calculated using equation (5) of Westaway (1990). The Cretaceous reference direction (note 1) is for Ramon in Israel (Ron 1987). The Jurassic reference direction (2) assumes 30° absolute rotation of the African plate, consistent with Sclater *et al.* (1977). Notes 3–5 denote subsets of data analysed in the text.

aceous magnetization vectors have $\alpha_0 = 50°$. Their anticlockwise rotation constrains $\Psi < 50°$. Thus, $32° < \Psi < 50°$.

One may consider together the rotations of magnetization vectors embedded in Jurassic ($\alpha_0 = 60°$; $\alpha = 115°$; note 3 in Table 1) and Cretaceous ($\alpha_0 = 50°$; $\alpha = 80°$; note 4) rocks in the Lebanon mountains. If all deformation has been caused by the DSFZ, equation (A33) can be applied. It gives $\Psi = 38°$, which from (A31) requires $\zeta = 2.5$, above the limit of 2 (Hancock & Atiya 1979). However, the uncertainties in the α_0 and α values cause ±12° uncertainty in Ψ (giving a 24–50° range), broader than the 32–50° limits already established. Although localities northeast of this stepover deformed during Mesozoic time (e.g. Lovelock 1984, Sawaf *et al.* 1993), it is unclear whether the Lebanon mountains were affected. However, regardless of whether some rotation of these Jurassic magnetization vectors occurred before Cretaceous time and was unrelated to the DSFZ, in this particular case equation (A33) does not provide useful constraint.

Table 2 lists solutions for the Cretaceous magnetization in the Lebanon mountains alone. $\Psi = 34°$ gives realistic parameters, including plate velocity $2V$ ~7.1 mm yr^{-1} and k ~0.06, predicting ~7 km of slip on the Yammouneh fault in 15 Myr, with shear strain $\gamma \sim -1.5$ and shortening factor $\zeta \sim 2.0$ in the Lebanon mountains. Because this preferred solution deflects $\alpha_0 = 60°$ to $\alpha = 109°$, it is also consistent with the Jurassic magnetizations, given their uncertainties (Table 1). The cross-bedding dips in the Grès du Liban have $\alpha = 120°$. Using (A24), their initial orientation α_0 was 65° or N35°W, indicating ~55° of anticlockwise rotation. This north-northwest paleoflow is roughly as expected.

The ~65° rotation of the Cretaceous magnetization near Mount Hermon ($\alpha_0 = 50°$; $\alpha = 115°$; note 5 in Table 1) instead requires $\zeta \sim 2.7$. This more intense deformation has presumably occurred because this part of the Anti-Lebanon mountains is narrower (with lower H) than the Lebanon mountains (Fig. 2).

The San Andreas Fault Zone in the Los Angeles area: observations

The San Andreas fault zone (SAFZ) takes up most of the ~50 mm yr^{-1} of right-lateral motion between the Pacific (PA) and North American (NA) plates, typically trending ~N40–45°W. Within the Big Bend stepover near Los Angeles, the San Andreas fault steps leftward by ~150 km, threading through complex structure where reverse faults in the E-trending Transverse ranges (Fig. 3) indicate substantial north–south shortening during Neogene time. Active shortening in the western Transverse ranges is indicated by their seismicity and structure (e.g. the Ventura basin—see Yeats 1983), and geomorphological (e.g. Rockwell *et al.* 1984) and geodetic (e.g. Feigl *et al.* 1993) observations.

The SAFZ began to form around 25 Ma when the adjoining plates first made contact, following subduction of the intervening Farallon (FA) plate. Stock & Hodges (1989) estimated that at ~20 Ma the SAFZ was ~400 km long, with its southern end of the PA–FA–NA triple junction near Los Angeles. Subduction of FA continued farther south, beneath southern California and Baja California. During ~20–10 Ma, when the PA–NA motion was at ~25 mm yr^{-1} towards ~N40°W, this triple junction migrated southeast to southernmost Baja California, such that at ~10 Ma this plate boundary was ~2100 km long. During ~10–5 Ma the plate motion adjusted to ~50 mm yr^{-1} towards ~N65°W, before adopting its present sense and rate around 5 Ma. During ~10–5 Ma, this motion was thus partitioned between right-lateral strike-slip west of Baja California and oblique extension in the Gulf of California. Around 5 Ma the modern plate boundary developed in the Gulf, comprising right-lateral transform faults between oceanic spreading centres. Stock & Hodges (1989) estimated that 175 km of oceanic crust has formed there since 3.4 Ma, indicating PA–NA motion at 51 mm yr^{-1}. De Mets *et al.* (1990) deduced 48 mm yr^{-1} by a similar calculation with slightly different parameters.

Most of the plate motion in southern California since ~5 Ma has been taken up on the San Jacinto and southern San Andreas faults. The 160 km offset of parts of a distinctive igneous body (Frizzell *et al.* 1986) indicates that their combined slip rate has been ~32 mm yr^{-1}, about two thirds of the PA–NA motion. The rest appears to be taken up mainly on right-lateral faults in the Eastern California Shear Zone (ECSZ) (Fig. 3), which slips at ~12 mm yr^{-1} (Sauber *et al.* 1994). The San Jacinto fault has slipped no more than ~24 km (Sharp

Table 2. Deformation since 15 Ma in the Lebanon mountains

Ψ (°)	ζ	k	h (Myr^{-1})	g (Myr^{-1})	V (mm yr^{-1})	v_s (mm yr^{-1})	v_s/V	u (°)	X_1 (°)	E_1 (Myr^{-1})	E_2 (Myr^{-1})
32	1.87	0.000	−0.0418	−0.0669	3.15	3.15	1.000	+28.7	61	−0.0603	0.0185
34	2.03	0.062	−0.0472	−0.0700	3.56	3.38	0.948	+30.1	62	−0.0658	0.0186
36	2.23	0.119	−0.0536	−0.0738	4.04	3.65	0.902	+31.7	63	−0.0724	0.0188
38	2.50	0.170	−0.0612	−0.0783	4.62	3.98	0.861	+33.7	64	−0.0803	0.0191
40	2.88	0.217	−0.0705	−0.0840	5.32	4.39	0.824	+36.1	65	−0.0901	0.0196

ζ is calculated from ψ using (A31) with $\alpha_0 = 50°$ and $\alpha = 80°$; k is calculated from Ψ using (A30) with $\theta = 32°$; h is calculated from ζ using (A25) with $t = 15$ Myr; g is calculated from Ψ and h using (A28); V (half the estimated relative plate velocity) is calculated from h using (A4) with H (the width of the push-up mountain range) 40 km; V_s (the estimated shortening rate across each range, in the Ψ-direction) is calculated from V, θ and k using (A6); v (the estimated rotation of a rigid circular inclusion) is calculated using (A8). E_1 and E_2, the principal shortening and extensional strain rates parallel and perpendicular to X_1, are calculated using (A9) and (A10).

1967), at a rate of ~5 mm yr^{-1} if time-averaged since 5 Ma. A ~27 mm yr^{-1} slip rate this seems likely on the southern San Andreas fault. Trenching establishes that its slip rate since 14 ka has indeed been 24.5 ± 3.5 mm yr^{-1} (Weldon & Sieh 1986).

The San Jacinto fault merges with the San Andreas fault near San Bernardino. The nearby San Gabriel fault (Fig. 3) became active after 10 Ma, and slipped ~40–60 km before ~5 Ma (e.g. May *et al.* 1993), when activity switched to the subparallel part of the San Andreas fault. Moving farther north, the San Andreas fault turns anticlockwise at the Big Bend: initially to ~N65°W along the northeast flank of the San Gabriel mountains, then briefly to ~N80°W, before resuming its NW-trend across Carrizo plain. Trenching reveals the Holocene seismicity here also, including Pallett Creek beside the San Gabriel mountains and Wallace Creek in Carrizo plain (Fig. 3). Pallett Creek has more earthquakes, but the slip each time is less. Given the available information (from Sieh 1978, Sieh 1984, Sieh & Jahns 1984 and Sieh *et al.* 1989), I estimate the ratio of slip rates between these localities as ~0.7 ± 0.2, giving the value of k. The trenching at Wallace Creek (Sieh & Jahns 1984) indicates a 34 mm yr^{-1} slip rate on the northern San Andreas fault (since 3.7 ka), similar to the combined slip rate on the southern San Andreas and San Jacinto faults south of the Big Bend. Correlation of Miocene and older features in the San Joaquin and La Honda basins (Fig. 3) constrains the displacement on the northern San Andreas fault to 320 km (Stanley 1987). About 240 km of this has developed since ~7 Ma at 34 mm yr^{-1} time-averaged rate, consistent with the Holocene slip rate from trenching; the rest occurred during ~23–7 Ma.

The left-lateral Garlock fault branches east-northeast from the San Andreas fault within the Big Bend (Fig. 3), and persists for ~250 km with concave-southward curvature with radius ~400 km. Its displacement is indicated by the ~55 km length of the Koehn Lake pull-apart basin (Fig. 3), and by offsets of older features displaced by 64 km (Smith 1962) or 74 km (Michael 1966). Early studies believed that the Garlock fault pre-dates the San Andreas fault (e.g. Hill & Diblee 1953), even suggesting that the Big Bend was caused by its left-lateral slip. Later work (e.g. Astiz & Allen 1983) suggests instead that the Garlock fault is younger. Compilations of data by Anderson (1979) and Bird & Rosenstock (1984) place its slip rate in the range 4–14 mm yr^{-1}; it is thus poorly constrained by direct observation.

The stress field gives an independent estimate of k for the Big Bend. Sonder (1990) deduced that the principal compressive stress is N14 ± 12°E, giving $X_1 = 101 \pm 12°$ with u-axis S65°E. Ψ from (A11) is thus 112 ± 24°. With $\theta = 20°$, equation (A30) gives $k = 0.80 + 0.15/-0.21$, consistent with the trenching results. Geodetic measurements in the Mojave desert/Garlock fault area indicate a shortening direction of N20°E (e.g. Savage *et al.* 1981). Assuming it reflects deformation associated with the Big Bend, this observational estimate of $X_1 = 95°$ indicates $\Psi = 100°$ and hence $k = 0.88$ using (A30).

Paleomagnetic studies reveal a complex pattern of rotation near the Big Bend. The typical clockwise rotation of northward magnetization vectors from early Miocene time is ~80° in the western Transverse ranges (e.g. Kamerling & Luyendyk 1985) and ~40° in the eastern Transverse ranges (e.g. Carter *et al.* 1987). For ~120 km distance northeast from the part of the San Andreas fault that bounds the San Gabriel mountains, vectors in the Mojave block show 15 ± 11° of anticlockwise rotation (Terres & Luyendyk 1985). The San Gabriel block, between the San Andreas and San Gabriel faults (Figs. 3 and 4), shows the most complex deformation: vectors magnetized northward in early Miocene time have rotated ~40° clockwise; those from latest Miocene/early Pliocene time have rotated 16 ± 30° anticlockwise instead (Terres & Luyendyk 1985). To explain these rotations in opposite senses, geometrical models involving rigid blocks require two sets of faults (e.g. Luyendyk 1989). As these blocks rotate away from one another, gaps form with infinite extensional strain. This problem can be avoided by assuming distributed deformation.

The San Andreas Fault Zone in the Los Angeles area: interpretation

I regard the most recent phase of deformation around the SAFZ as post-5 Ma, including the anticlockwise rotation of the youngest magnetization in the San Gabriel block and 160 km displacement on the southern and northern San Andreas faults with V ~16–17 mm yr^{-1}. With a S65°E u-axis, θ in the San Gabriel area is ~20°, and the north direction has $\alpha = 115°$. The

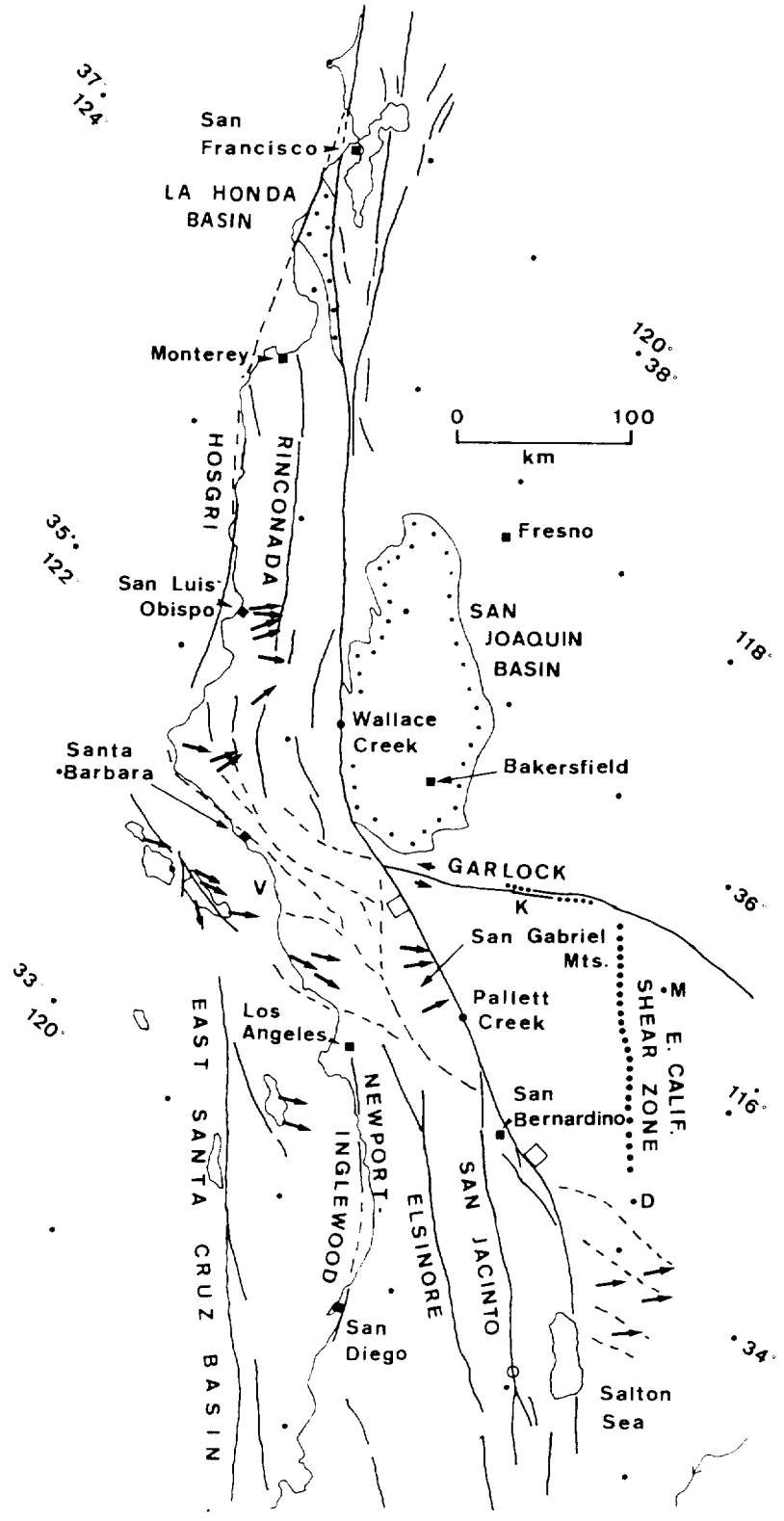

Fig. 3. Summary map of the San Andreas fault zone in central and southern California, including its leftward stepover in the Big Bend. Major strike-slip faults are shown by thick solid lines, including the left-lateral Garlock fault. The designated San Andreas fault runs from west of San Francisco, through the Wallace Creek and Pallett Creek trench sites, then southeastward to the eastern margin of the Salton Sea. In this study I designate its northern and southern parts as bounded by its intersection with the Garlock fault. Short arrows mark localities where magnetization vectors have rotated substantially clockwise. Open squares indicate parts of a distinctive igneous body, whose offset indicates the displacement on the San Jacinto and southern San Andreas faults (Frizzell *et al.* 1986). Thin line and dots outline the San Joaquin and La Honda basins, whose offset indicates the displacement on the northern San Andreas fault (Stanley 1987). Open circle southwest of the Salton Sea marks the Ocotillo Badlands stepover. K is the Koehn Lake (Cantil valley) pull-apart basin on the Garlock fault. M and D are the positions of the Mojave Desert and Deadman Lake geodetic markers (Feigl *et al.* 1993). V is the Ventura basin. Other information from Bird & Rosenstock (1984) and Wesnousky (1986).

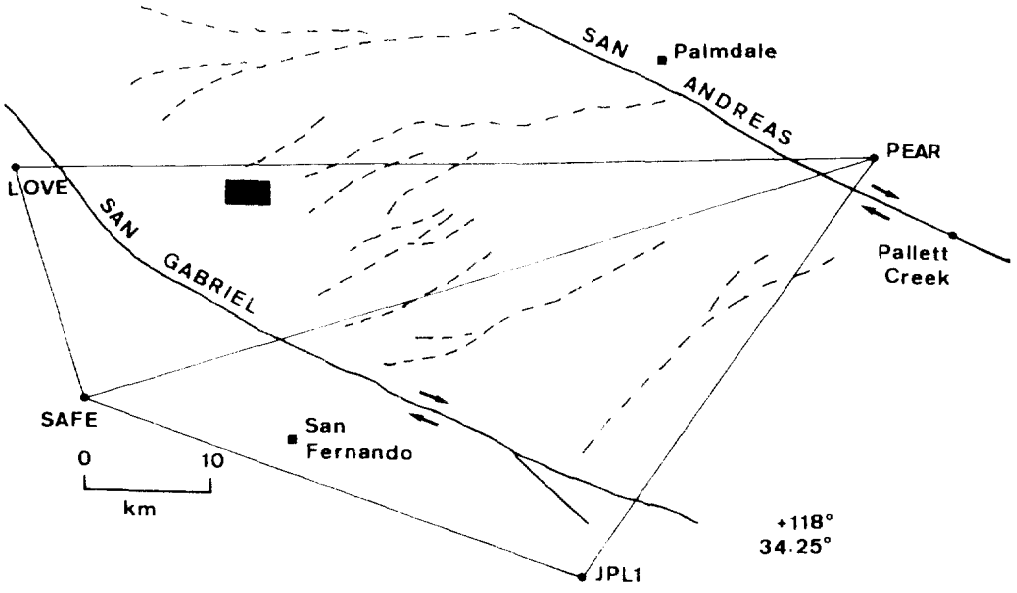

Fig. 4. More detailed map of the central San Gabriel block between the San Andreas and San Gabriel faults. Dashed lines are minor faults within this block, most of which have a component of left-lateral slip (some also have a component of shortening). Solid circle indicates the Pallett Creek trench site. Solid rectangle indicates the area where a small anticlockwise rotation of northward paleomagnetic vectors has occurred in the past few million years. Solid circles linked by thin lines are geodetic markers: PEAR is at Pearblossom, LOVE is at Loma Verde, SAFE is in the western San Fernando valley, and JPL1 is at the Jet Propulsion Laboratory in Pasadena. Information is from Terres & Luyendyk (1985) and Feigl *et al.* (1993).

Table 3. Deformation since 5 Ma in and around the San Gabriel mountains

Ψ (°)	ζ	k	b (Myr^{-1})	g (Myr^{-1})	V (mm yr^{-1})	v_s (mm yr^{-1})	γ, V	a (°)	λ_1 (°)	E_1 (Myr^{-1})	E_2 (Myr^{-1})
115	∞	0.78									
114	6.27	0.79	0.367	0.163	107.33	40.17	0.374	−23.4	102	0.384	0.017
112	2.78	0.80	0.208	0.083	59.87	22.07	0.369	11.8	101	−0.213	0.00080
110	2.09	0.82	0.147	0.053	42.97	15.63	0.364	7.7	100	−0.153	0.0058
105	1.56	0.85	−0.089	0.024	26.00	9.20	0.354	3.4	97.5	−0.090	0.0016
100	1.38	0.88	−0.065	0.011	18.97	6.60	0.347	1.6	95	−0.065	0.00050
98	1.34	0.89	−0.059	0.0082	17.15	5.92	0.345	1.2	94	−0.059	0.00029
95	1.29	0.91	0.051	0.0045	15.03	5.16	0.343	0.6	92.5	−0.052	0.000098
90	1.24	0.94	0.043	0.0000	12.50	4.27	0.342	0.0	90	−0.043	0.000000

H = 100 km, θ = 20°, α_0 = 115° and α = 120°. Other parameters are calculated as in Table 2.

observation that vectors with α_0 = 115° have rotated anti-clockwise thus means Ψ < 115°; using (A5) means Ψ > 90°. With θ = 20°, equations (A30) and (A12) require 0.78 < k < 0.94, imposing tighter bounds than the ~0.5–0.9 range from stress measurements and trenching. However the formal uncertainties in the paleomagnetic data mean maybe 15° of anticlockwise rotation, or possibly none at all.

For this deformation phase I adopt H = 100 km, from the dimensions of the Mojave block. Assuming α = 130° for α_0 = 115° requires high shortening factors, which seem unrealistic given the local geology. It is thus unlikely that magnetization vectors oriented northward at 5 Ma have rotated anticlockwise by as much as 15°. Table 3 lists solutions for 5° of rotation (α_0 = 115°, α = 120°) instead. The required shortening is now moderate, and realistic parameter values arise for a range of Ψ. My preferred solution with Ψ = 98° means V = 17 mm yr^{-1}, shortening factor ζ ~ 1.3, and [using (A26)] shear strain γ = 0.04.

With this solution, any vector with 0° < α_0 < 98° (i.e. S65°E to N17°E) when this deformation began will have rotated clockwise. Any older magnetization that had already rotated clockwise by >17° will thus have continued to rotate clockwise. This means that some of the substantial clockwise rotation of the early Miocene magnetization around the Big Bend may have occurred during the present deformation phase. However, with ζ = 1.3 and γ = 0.04, the maximum clockwise rotation during this phase is only ~9°, so vectors now oriented N80°E or N40°E would have pointed towards N72°E or N35°E at its start. Most of their clockwise rotation thus occurred earlier.

DISCUSSION

Evolution of the Dead Sea fault zone in Lebanon

As Walley (1988) and others have pointed out, a space problem occurs when the surroundings to the Lebanon stepover are regarded as rigid. Previous solutions (e.g. Freund *et al.* 1970, Ron 1987, Walley 1988, Ron *et al.*

1990, Khair *et al.* 1993) either require rigid body rotations in the surroundings to the Yammouneh fault or major displacements on other faults; neither view seems satisfactory. The models in Table 2 avoid this problem by distributed deformation. The predicted shortening in the Lebanon mountains is subparallel to the plate motion (Ψ = 34° for θ = 32°: N4°W against N2°W), causing a shortening factor ζ of ~2. These mountains are also predicted to have extended in the orthogonal direction, at a strain rate roughly 1/4 the shortening strain rate.

Most fold axes in the Lebanon mountains are now subparallel to the Yammouneh fault (Fig. 2). Hancock & Atiya (1979) suggested that they formed subperpendicular to the plate motion, and have since rotated anticlockwise. If so, their initial orientations were ~S87°W or α_0 = 122°. With $\zeta \sim 2$ and $\gamma \sim -1.5$, (A24) thus predicts $\alpha \sim 160°$. The region has thus indeed deformed sufficiently to deflect these fold axes subparallel to the Yammouneh fault and not rotated, or with α_0 say ~20° (initial strike ~N10°E) and rotated clockwise to $\alpha \sim 14°$. It is impossible in principle to distinguish between these possibilities using the available evidence, other than by intuition. If these folds are equivalent to the folds in the Ocotillo stepover mentioned earlier, then their axes most likely formed subparallel to the Yammouneh fault and have thus not rotated significantly.

To reduce the predicted shortening factor for the Lebanon mountains below ~2 requires smaller θ. Walley (1988) adopted a ~N5–10°E slip vector on the transform part of the DSFZ, which means $\theta \sim 20$–25°. With θ = 25°, α_0 = 50° and α = 80° require ζ = 1.5. The Sultan *et al.* (1993) Euler pole near 35°N 18°E predicts plate motion towards N7°E in Lebanon, indicating θ = 23°. However, the required 6.7° relative rotation would mean ~190 km of slip parallel to the DSFZ, more than is observed. A definitive solution for the kinematics of the Lebanon stepover will thus probably need more precise values of θ, α_0, α and ζ, which means more precise field and paleomagnetic studies. It is not clear which parameters are best constrained at present. The fit between theory and observation obtained in this study nonetheless suggests that the general principles governing this stepover have been resolved.

Evolution of the San Andreas fault zone

The maximum compressive stress subperpendicular to the San Andreas fault around the Big Bend has been explained as an effect of distributed deformation with high (~0.9) k. However, this stress component is also subperpendicular to this fault in central California (e.g. Zoback *et al.* 1987). Many people (e.g. De Mets *et al.* 1990) have noted that this fault trends at ~5° to the expected PA–NA motion. It is thus not a true transform fault, and can instead be regarded as a stepover with θ ~5° and k almost 1. Using (A30), the principal compressive stress is thus predicted subperpendicular to its strike, as is observed.

Earlier analysis showed that the large clockwise rotations of the oldest magnetization in the Transverse Ranges developed before the present deformation phase. To investigate this earlier time, Fig. 5 restores this most recent deformation. In Fig. 5(a) the northern San Andreas fault is assumed to slip at rate $2V$ = 34 mm yr^{-1}, restoring 170 km of slip in 5 Myr. South of the Big Bend, the southern San Andreas and San Jacinto faults are assumed to slip at the same rate. With k within the Big Bend almost 1, the 160 km offset of the truncated igneous bodies is thus restored at 5 Ma, when the southern end of the San Gabriel fault was near the northern end of the Elsinore fault.

Figure 5(a) thus leaves ~80 km of displacement from ~7–5 Ma given Stanley's (1987) interpretation of the northern San Andreas fault. Farther south, the San Gabriel fault was active immediately before 5 Ma, and slipped between 40 km and 55–60 km (May *et al.* 1993). The Elsinore fault seems to have slipped no more than ~5 km since 5 Ma, but has slipped ~40 km since middle Miocene time (e.g. Anderson 1979), suggesting ~35 km of late Miocene slip. I thus suggest that for a brief period before 5 Ma (lasting ~1–2 Myr), the San Gabriel and Elsinore faults took up most of the PA–NA motion in southern California. They connected to the northern San Andreas across an incipient Big Bend that was narrower than the modern feature. Restoring 60 km more displacement on these faults thus leads to the configuration in Fig. 5(b) around 7 Ma.

The Big Bend has thus migrated at rate V = 17 mm yr^{-1} relative to both plates since 7 Ma. It was thus north of its present position relative to the Pacific plate at that time, with its northern end north of the western Transverse ranges. Assuming constant k, the predicted shortening rate perpendicular to this bend is $H\dot{h}$ or 100 km × ~0.06 M yr^{-1} = 6 mm yr^{-1}, giving ~40 km of shortening in 7 Myr. On the Pacific side of the Bend, this shortening has presumably been taken up mainly in the western Transverse ranges. However, it is impossible to accept such dramatic shortening in the Mojave block on its North American side.

The Mojave block may instead have been deflected away from the bend in the San Andreas fault by slip on the Garlock fault. Because this fault is oriented at ~45° to the required shortening direction, it would need to slip left-laterally at a rate ~$H\dot{h}$/sin(45°) or ~8.5 mm yr^{-1} to achieve this. It is thus expected to have slipped ~60 km since 7 Ma, the amount observed. It is, of course, not possible for the Mojave block to remain rigid during this slip: its shape would have to change to accommodate the bend in the San Andreas fault, so this calculation is approximate. However, it does provide a first-order explanation for why the Garlock fault is present, when it formed (~7 Ma), and why it has slipped ~60 km; issues that were previously unresolved.

The restoration of ~230–240 km of slip in Fig. 5(b) roughly lines up the flanks of the eastern and western Transverse ranges, consistent with the view that they were created during earlier deformation. The reconstructions in Fig. 5 differ radically from previous attempts, such as fig. 13 of May *et al.* (1993) or fig. 3 of

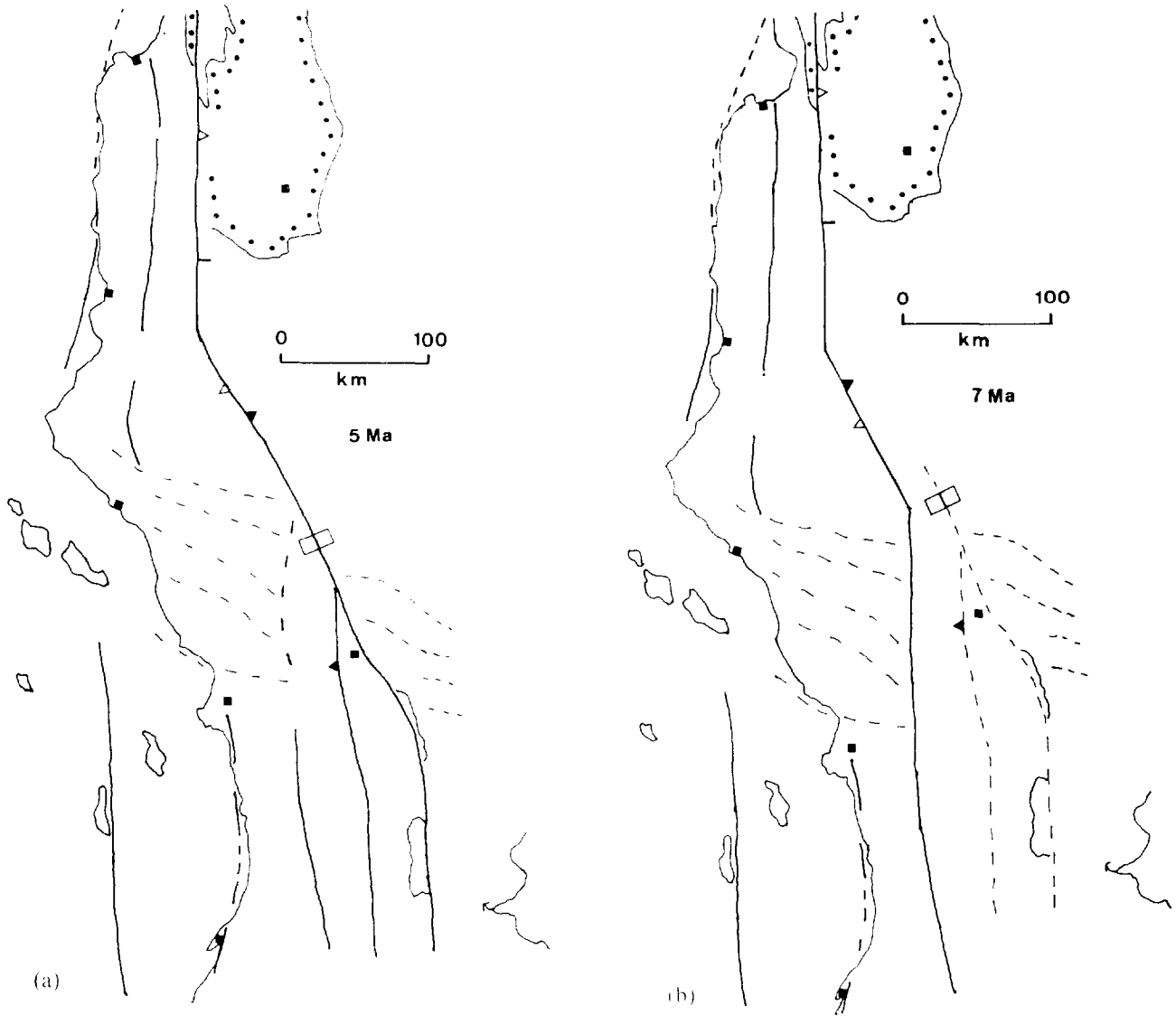

Fig. 5. Cartoons showing California at 5 Ma (a) and 7 Ma (b), with slip on right-lateral faults and distributed deformation restored as discussed in the text. Solid squares denote towns: from top to bottom, Monterey, Bakersfield, San Luis Obispo, Santa Barbara, San Bernadino, Los Angeles and San Diego. Thin lines with dots are the San Joaquin and La Honda basins. Open squares mark the igneous body discussed by Frizzell *et al.* (1986), which constrains the 160 km displacement that is restored in (a). Solid triangles denote the restored positions of points that are now juxtaposed at the Pallett Creek trench site. Open triangles are the same for Wallace Creek. Short bar is the estimated initial position of the intersection between the San Andreas and Garlock faults. Thick lines are major right-lateral faults, including the San Gabriel fault (which ceased to be active at 5 Ma) that is dashed in (a). Fine dashed lines indicate the position and contemporaneous structural trend of the Transverse ranges. The full estimated ~40 km post-7-Ma shortening in the western Transverse ranges has not been restored. If it were, their northern edge would be farther north, closer in line with the restored northern edge of the eastern Transverse ranges. Symbols shown are compatible with Fig. 3.

Luyendyk *et al.* (1980), which restored clockwise rigid-body rotations of blocks within the Transverse ranges.

Using Fig. 5(b) one can begin to address what was happening before 7 Ma. In the north, where the San Andreas fault already existed, its time-averaged slip rate is estimated from Stanley's (1987) observations as ~5 mm yr^{-1}. Most of the plate motion was thus taken up on faults farther west, such as the Hosgri and Rinconada faults. Offset bathymetric features near Monterey indicate that the Hosgri fault has indeed slipped ~110 km (Howell *et al.* 1980). In the south, the plate motion was presumably originally also taken up on offshore strike-slip faults, until the plate boundary began to adjust east around ~10 Ma when the extension in the Gulf of California started. Inspection of Fig. 5(b) indicates that a leftward stepover existed in the plate boundary across the Transverse ranges before 7 Ma, as at present. I suggest that the dramatic clockwise rotation of the magnetization vectors there occurred at this time.

To quantify this earlier deformation, the structural trend in the Transverse ranges is regarded as the u-axis within the stepover: its direction of no length change and no rotation. This is equivalent to assuming that the major active folds within these ranges are analogous to the folds in the other study localities, which seems intuitively reasonable. If the time-averaged plate motion before 7 Ma is assumed towards N45°W, the N80°W u-axis means $\theta = 35°$. The rotation of magnetization vectors from N to N80°E in the western Transverse ranges thus means $\alpha_0 = 100°$ and $\alpha = 20°$. The north–

Table 4. Estimates of present day velocity gradient tensor elements for the San Gabriel block

	E_1 (Myr^{-1})	E_2 (Myr^{-1})	X_1	χ_z ($°Myr^{-1}$)
	(1) *Geodetic results*			
Garlock fault/Mojave area	-0.14 ± 0.03	0.02 ± 0.03	N20°E	Not resolved
	(2a) *Geodetic results: observed*			
PEAR–SAFE–LOVE	-0.21 ± 0.06	0.16 ± 0.03	N86°W	-8.0 ± 4.4
PEAR–SAFE–JPL1	-0.11 ± 0.05	0.16 ± 0.04	N28 ± 8°W	-20.6 ± 3.4
PEAR–DEAD–MOJA	-0.02 ± 0.02	0.10 ± 0.03	N25 ± 10°E	-9.8 ± 2.4
	(2b) *Geodetic results: modelled*			
PEAR–SAFE–LOVE	-0.13 ± 0.06	0.00 ± 0.03	N96°W	$+5.4 \pm 4.4$
PEAR–SAFE–JPL1	-0.01 ± 0.05	0.11 ± 0.04	N92 ± 8°E	-1.6 ± 3.4
PEAR–DEAD–MOJA	-0.03 ± 0.02	0.06 ± 0.03	N45 ± 10°E	-3.8 ± 2.4
	(3) *Preferred results of this study*			
San Gabriel/Mojave Blocks	−0.059	0.00029	N21°E	−0.47

E_1 and E_2 are the shortening and extensional eigenvalues of the strain rate tensor. X_1 is the azimuth of the shortening eigenvector, expressed in geographical coordinates χ_z is the vertical vorticity (anticlockwise positive). Geodetic results are from Savage *et al.* (1981) (1), and Feigl *et al.* (1993) (2).

south width of these ranges is now ~120 km; it is estimated to have been ~160 km before the ~40 km of shortening estimated since 7 Ma, making $H = 80$ km. With Ψ assumed to be 140°, (A30) gives $k = 0.134$, and from (A31) the required shortening factor is 3.88. Using (A25) and (A28), over 15 Myr this shortening factor requires strain rates $h = 0.0904\ Myr^{-1}$ and $g = 0.1077\ Myr^{-1}$. With V estimated as 12.61 mm yr^{-1} from (A4), ~25 mm yr^{-1} of time-averaged plate motion is accounted for. This deduction that most of the clockwise rotation of the magnetization in the western Transverse ranges occurred before latest Miocene time is of course not new (e.g. Terres & Luyendyk 1985). However, it was previously proposed in an ad hoc way, rather than as a result of general considerations.

Interpretation of geodetic results around the Big Bend

Since the early 1980s, space geodetic methods have been used to observe the active deformation around the SAFZ. Results of eight years of this work, spanning its ~700 km length south of Monterey, are now available (e.g. Feigl *et al.* 1993), and can in principle be compared with my predictions. However, the sparse geodetic network (see e.g. fig. 1 of Feigl *et al.* 1993) includes few markers <100 km apart. The relative motions of many adjacent markers thus involve components of both distributed deformation and localized strike-slip, which need to be isolated. Feigl *et al.* (1993) did this by subtracting effects of a slip model for the major strike-slip faults. This included a 34 mm yr^{-1} slip rate on the San Andreas fault within the Big Bend, which exceeds my ~30.5 mm yr^{-1} estimate in Table 3. Their model slip rate for the Garlock fault (10 mm yr^{-1} is instead higher than mine (~8.5 mm yr^{-1}). They assumed that slip on these and other major strike-slip faults is continuous in the lower crust, the faults being locked in the upper crust between major earthquakes. Their model also omitted the ECSZ, one of the most active fault zones in southern California (Sauber *et al.* 1994).

Feigl *et al.* (1993) processed the geodetic data in the standard way using triangulation. The three triangles of markers adjacent to the Big Bend link points PEAR (Pearblossom), SAFE (San Fernando) and LOVE (Loma Verde); PEAR, SAFE and JPL1 (Pasadena); and PEAR, MOJA (Mojave Desert) and DEAD (Deadman Lake). The PEAR–DEAD–MOJA triangle (Figs. 3 and 4) is within the Mojave block northeast of the San Andreas fault, except for its eastern edge that straddles the ECSZ. The other two triangles (Fig. 4) link points southwest of this fault with PEAR with its northeast side. For these triangles the modelled deformation rates and senses (taking account of the model for San Andreas fault slip) differ more than for the other triangle that is within the Mojave block (Table 4).

The geodetic observations from the PEAR–DEAD–MOJA triangle predict a similar orientation of the strain rate tensor to my theory, including an extensional strain rate negligibly different from zero. Their shortening strain rate is less than mine, presumably because my estimate neglects the deformation associated with slip on the Garlock fault. The less impressive agreement between their modelled results for PEAR–DEAD–MOJA and my prediction may instead be because they have omitted the ECSZ.

Because the two triangles that are mainly SW of the San Andreas fault (PEAR–SAFE–LOVE and PEAR–SAFE–JPL1) cover tectonically equivalent areas, their deformation rates and senses should be similar. However, both their observed and modelled deformations differ substantially (Table 4). Nonetheless, if one averages together the modelled geodetic results for both triangles, results similar to my predictions are obtained. This averaging thus seems to have led to a more robust result than is obtained when the two sets of data are treated separately, suggesting that the differences between their geodetic results may be caused by uncertainties in the observations.

Role of second-order faults in stepovers

The surroundings to the Yammouneh fault (Fig. 2) and the San Gabriel block (Fig. 3) both contain second-

Table 5. Interpretation of secondary faults

Zone	α_{obs} (δ)	$\alpha_0(\alpha_{obs})$ (°)	$\alpha_{0,pred}$ $\varphi_1=30°$ (°)	$\varphi_1=45$ (°)
Lebanon mountains	140 ± 15	81+27/−13	92	107
San Gabriel block	55 ± 15	63−13/−15	64	49

Deformation is restored [from α_{obs} to $\alpha_0(\alpha_{obs})$] using (A24) with ζ = 2.0 and γ = 1.5 for the Lebanon mountains and ζ = 1.3 and γ = + 0.04 for the San Gabriel block (post-5-Ma). Predicted initial strike of secondary faults $\alpha_{0,pred}$ is calculated as $X_1 + \varphi_1$ for φ_1 = 45° and φ_1 = 30°, for X_1 = 62° (Lebanon) and 94° (San Gabriel)

order strike-slip faults, with the opposite slip sense to the major faults. The left-lateral set in the San Gabriel block typically strike S60 ± 15°W, indicating α = 55°. They are typically ~10 km apart and appear offset by no more than ~2 km (e.g. Terres & Luyendyk 1985). The right-lateral set in the Lebanon mountains typically strike S70 ± 15°W, indicating α = 140°. They are typically ~5 km apart and appear offset by no more than ~1 km (e.g. Hancock & Atiya 1979).

Standard theory for an ideal elastic body predicts that shear failure is expected at 45° to the principal axes of the stress tensor, the direction of greatest shear stress. However, internal friction within rocks can cause this angle to adjust to ~30° to the principal compressive stress (e.g. Segall & Pollard 1980), which I equate to the azimuth of the shortening eigenvector. Table 5 compares the initial orientations for these fractures calculated using these criteria with the values expected from the present day orientations of these features. The agreement is indeed better with the 30° criterion than for 45°.

This interpretation of the second-order faults differs considerably from their role in rigid block models, in which these faults were fundamental to allowing the adjoining blocks to rotate around vertical axes. In my present model, they appear instead as a minor detail. Although the local velocity field near any such fault will be affected by it, and thus differs from what it would be if deformation were precisely uniform, the perturbation appears insufficient to have any significant effect.

Wider implications

Segall & Pollard (1980) and Rodgers (1980) were the first to analyse the elastic stress field near strike-slip fault segments that are offset out of line. They treated the stress field in the vicinity of the jog as imposed externally, with σ_1 (the maximum compressive stress) oriented oblique (~25°) to the transform fault segments and σ_3 (the minimum compressive stress) in the orthogonal horizontal direction. They deduced that the mean horizontal stress $[(\sigma_1 + \sigma_3)/2]$ decreases near an antidilatational jog on the outward sides of both transform faults, whereas the shear stress $[(\sigma_1 - \sigma_3)/2]$ increases within the jog. Reches (1987) showed that in an ideal elastic–brittle material this stress field will cause the tips of the transform faults to propagate outward, away from each other; this is not observed in the real Earth. He showed instead that with a plastic rheology in the upper crust, these tips are instead deflected towards each other, eventually linking across a zone of distributed deformation. This rheological assumption thus predicts the general behaviour that is observed in the real Earth.

The analysis in this study suggests that the stress field at a stepover is determined by its geometry, and is thus not externally imposed. The main factor affecting this orientation is the value of k. Where k is small, as has been estimated for the Yammouneh fault, σ_1 is at ~30° to the plate motion, roughly as assumed by Segall & Pollard (1980) (for the Lebanon mountains with k ~0.06, X_1 is 62°; θ is 32°, so $X_1 - \theta$ is 30°). However, where k is large, as in the modern Big Bend, σ_1 is subperpendicular to the internal fault and thus strongly oblique to the plate motion (X_1 is ~90°; θ is ~20°, so $X_1 - \theta$ is ~70°).

The suggestion, from Reches (1987), that the bounding transform fault segments propagate inward, and eventually meet to create a throughgoing internal fault, raises the possibility that the formation of stepovers is a two stage process. In the first stage, when the faults have not yet linked and there is no throughgoing fault, k can be expected to be zero. After this fault has formed, k is instead much larger.

To assess this possibility, consider the ideal stepover in Fig. 1(a). After time t the adjoining transform faults slip by distance $2Vt$. The plate 2 side of the transform fault at point K will not move. The displacement at point K is thus Vt, so the slip rate is V. In this ideal model, the slip rate thus decreases uniformly from $2V$ at point Q to V at point K, then immediately to zero between points K and J. This is unrealistic; it is more likely that the decrease in displacement from Vt to zero will occur over a finite distance (say, K–S) along the internal fault. If this distance equals Vt, then the time t_0 required for both inward-propagating faults J–R and K–S) to meet at the mid-point of the stepover is

$$t_0 = \frac{L}{2V}. \quad (1)$$

For instance, for the Bekaa valley ($2V$ = 7 mm yr^{-1}, L = 100 km), t_0 is ~14 Myr. Before time t_0 is reached, the stepover can be regarded as having a low-k central part (R–S) whose length decreases gradually to zero.

This calculation thus raises the possibility that the throughgoing Yammouneh fault, and the associated sense of deformation in its surroundings, are very young. The Lebanon stepover may have formed with distributed deformation with k ~0 lasting ~14 Myr, until the adjoining transform fault segments linked, followed by a phase that has so far lasted just ~1 Myr with much higher k. The 7 km length of the Yammouneh pull-apart basin may thus indicate present-day slip rate $2V$ ~7 mm yr^{-1} since ~1 Ma, indicating k near 1. Supporting evidence for this suggestion is provided by comparing the historical seismicity of the Bekaa valley and other parts of the DSFZ. The seismicity since ~2 Ka indicates that the Yammouneh fault and the northern DSFZ have similar slip rates (Westaway 1994). The

main difference is that the Yammouneh fault has fewer great earthquakes at longer intervals. This contrasts with the Big Bend, where the adjoining transform faults have fewer great earthquakes (Sieh *et al.* 1989).

Taking the present-day value of k for the Lebanon stepover as 0.8, near the upper bound of 0.85 (A12), gives Ψ and X_1 only slightly less than 90°, or ~N50°W. Using (A9) with $V = 3.5$ mm yr^{-1} $H = 40$ km and $\theta = 35°$, the Lebanon mountains are predicted to be shortening subperpendicular to this fault at strain rate ~0.05 Myr^{-1} or $\sim 1.5 \times 10^{-15}$ s^{-1}. The predictions for $k <\sim 0.1$ would instead be $\Psi \sim 40°$ and $X_1 \sim 65°$, or ~N10°W and ~N35°W. If this suggestion is correct, then Table 2 estimates the time-averaged deformation during its first phase, from ~15 to ~1 Ma. It could be tested by *in situ* stress measurements (to measure present-day X_1) or surveying (to measure present-day Ψ).

In the San Andreas fault zone, the low-k deformation phase lasted ~15 Myr (~22 to ~7 Ma) across a zone with L ~200 km. From (1) this suggests that no surrounding transform fault active at the time has slip rate $>\sim 15$ mm yr^{-1}. This is consistent with the existence of several subparallel active strike-slip faults on either side of the Transverse ranges, and with the view that for much of this time the PA–NA motion was only ~25 mm yr^{-1} (e.g. Stock & Hodges 1989). Short low-k stepovers, like the Ocotillo badlands, would instead be short-lived, evolving to high-k stepovers before much deformation can occur in their surroundings. Their first phase of deformation may thus easily be missed.

Finally, this study contradicts the widely held view that clockwise rotation is always expected around right-lateral strike-slip faults and *vice versa*. No rotation is expected around transform faults. Depending on their orientation, vectors embedded in deformation around stepovers may instead rotate in either sense, irrespective of the slip sense and polarity of the stepover, as is strikingly illustrated by the paleomagnetic data from the Big Bend. The probable reason why this effect has not been noticed before, or has been attributed to observational error (e.g. Jackson & Molnar 1990) is the small angular width of the quadrant with the 'unexpected' rotation sense. For the time-averaged deformation in the Lebanon mountains with $\Psi = 34°$, the 0–34° azimuth range with this unexpected sense is <20% of the total, and is so small that no vector within it can ever rotate much. For instance, a vector magnetized northward at 15 Ma ($\alpha_0 = 30°$) would now point towards $\alpha = 27°$, a 3° rotation that would hardly be measurable. The high present-day k value in the Big Bend and the associated $\Psi = 98°$ means that 46% of vector orientations instead show the 'unexpected' rotation. It is fortunate that the vectors magnetized northward around 5 Ma lie within this range, enabling this rotation to be observed.

CONCLUSIONS

A simple quantitative model, incorporating deformation, is applied to stepovers in strike-slip fault zones. The deformation sense depends on the angle θ between the internal strike-slip fault within the stepover and the adjoining transform faults, and k, the ratio of their slip rates. The boundaries to the deforming zone converge at an angle Ψ to the internal fault, which depends on θ (usually ~30°) and k. This Ψ-direction also bounds quadrants in which vectors rotate in opposite senses. This theory accounts for several previously puzzling observations in a consistent manner. It explains why vectors embedded in the deformation in the Lebanon mountains around the stepover on the Dead Sea fault zone have rotated anticlockwise through different angles depending on their initial orientations. It also explains the observed anticlockwise rotation of paleomagnetic vectors embedded in the youngest rocks within the Big Bend stepover, and the observed stress field with principal compressive stress subperpendicular to the San Andreas fault as consequences of high (~0.9) k. It predicts that the Garlock fault became active at ~7 Ma and has since slipped ~60 km at an ~8.5 mm yr^{-1} rate, while ~40 km of shortening has occurred in the western Transverse ranges. It suggests strongly that the present-day structure is the result of an initial deformation phase with low k (~0) before ~7 Ma, followed by the present phase with high (~0.9) k. The Lebanon stepover also shows evidence for recent evolution from low to high k. Such behaviour is predicted by theoretical rock mechanics models in which the upper crust deforms plastically.

REFERENCES

Anderson, J. D. 1979. Estimating the seismicity from geological structure for seismic risk studies. *Bull. seism. Soc. Am.* **69**, 135–158.

Astiz, L. & Allen, C. R. 1983. Seismicity of the Garlock fault, California. *Bull. seism. Soc. Am.* **73**, 1721–1735.

Aydin, A. & Nur, A. 1982. Evolution of pull apart basins and their scale independence. *Tectonics* **1**, 91–105.

Aydin, A. & Nur, A. 1985. The types and role of stepovers in strike-slip tectonics. In: *Strike-slip Faulting, Basin Formation, and Sedimentation* (edited by Biddle, K. T. & Christie-Blick, N.). *Spec. Publs Soc. econ. Palaeont. Miner.* **37**, 35–44.

Bird, P. & Rosenstock, R. W. 1984. Kinematics of present crust and mantle flow in southern California. *Bull. geol. Soc. Am.* **95**, 946–957.

Carter, J. N., Luyendyk, B. P. & Terres, R. R. 1987. Neogene clockwise tectonic rotation of the eastern Transverse Ranges, California, suggested by paleomagnetic vectors. *Bull. geol. Soc. Am.* **98**, 199–206.

Chaimov, T. A., Barazangi, M., Al-Saad, D., Sawaf, T. & Gebran, A. 1990. Crustal shortening in the Palmyride fold belt, Syria, and implications for movement along the Dead Sea fault system. *Tectonics* **9**, 1369–1386.

Clark, M. M., Grantz, A. & Rubin, M. 1972. Holocene activity of the Coyote Creek fault as recorded in sediments of Lake Cahuilla. *U.S. Geol. Surv. Profess. Paper* **787**, 112–130.

Crowell, J. C. 1974. Origin of the late Cenozoic basins in southern California. In: *Modern and Ancient Geosynclinal Sedimentation* (edited by Dott, R. H. & Shaver, R. H.). *Spec. Publs Soc. econ. Palaeont. Miner.* **22**, 190–204.

Cutler, J. & Elliott, D. 1983. The compatibility equations and the pole to the Mohr circle. *J. Struct. Geol.* **5**, 287–297.

De Mets, C., Gordon, R. G., Argus, D. F. & Stein, S. 1990. Current plate motions. *Geophys. J. Int.* **101**, 425–478.

Feigl, K. L., Agnew, D. C., Bock, Y., Dong, D., Donnellan, A., Hager, B. H., Herring, T. A., Jackson, D. D., Jordon, T. H., King, R. W., Larsen, S., Larson, K. M., Murray, M. H., Shen, Y. & Webb, F. H. 1993. Space geodetic measurement of crustal defor-

mation in central and southern California, 1984–1992. *J. geophys. Res.* **98**, 21,677–21,712.

Freund, R., Garfunkel, Z., Zak, I., Goldberg, M., Weissbrod, T. & Derin, B. 1970. The shear along the Dead Sea rift. *Phil. Trans. R. Soc. Lond. Ser. A.* **267**, 107–130.

Frizzell, V. A., Mattinson, J. M. & Matti, J. C. 1986. Distinctive Triassic megaporphyritic monzogranite: Evidence for only 160 km offset along the San Andreas fault, southern California. *J. geophys. Res.* **91**, 14,080–14,088.

Garfunkel, Z. 1981. Internal structure of the Dead Sea leaky transform (rift) in relation to plate kinematics. *Tectonophysics* **80**, 81–108.

Gregor, C. B., Mertzman, S., Narin, A. E. M. & Negendank, J. 1974. Paleomagnetism and the Alpine tectonics of Eurasia 5: The paleomagnetism of some Mesozoic and Cenozoic volcanic rocks from the Lebanon. *Tectonophysics* **21**, 375–395.

Hancock, P. L. & Ativa, M. S. 1979. Tectonic significance of mesofracture systems associated with the Lebanese segment of the Dead Sea transform fault. *J. Struct. Geol.* **1**, 143–153.

Hanks, T. C. & Kanamori, H. 1979. A moment-magnitude scale. *J. geophys. Res.* **84**, 2348–2350.

Hill, M. L. & Diblee, T. W. 1953. San Andreas, Garlock and Big Pine faults, California. *Bull. geol. Soc. Am.* **64**, 443–458.

Holt, W. E. & Haines, A. J. 1993. Velocity fields in deforming Asia from the inversion of earthquake-released strains. *Tectonics* **12**, 1–20.

Hornafius, J. S., Luyendyk, B. P., Terres, R. R. & Kamerling, M. J. 1986. Timing and extent of Neogene tectonic rotation in the western Transverse Ranges, California. *Bull. geol. Soc. Am.* **97**, 1476–1487.

Howell, D. G., Crouch, J. K., Greene, H. G., McCulloch, D. S. & Vedder, J. G. 1980. Basin development along the late Mesozoic and Cainozoic California margin: a plate tectonic margin of subduction, oblique subduction, and transform tectonics. In: *Sedimentation in Oblique-Slip Mobile Zones* (edited by Ballance, P. F. & Reading, H. G.). *Spec. Publs Int. Ass. Sediment.* **4**, 43–62.

Jackson, J. A. 1988. Rock around the clock. *Nature* **334**, 195–196.

Jackson, J. A. & Molnar, P. 1990. Active faulting and block rotations in the western Transverse Ranges, California. *J. geophys. Res.* **95**, 22,073–22,087. (Correction: **96**, 2203, 1991.)

Jennings, C. W. & Strand, R. G. 1969. Geologic map of California, Los Angeles Sheet, 1:250,000 scale. California Division of Mines and Geology, San Francisco.

Kamerling, M. J. & Luyendyk, B. P. 1985. Paleomagnetism and Neogene tectonics of the northern Channel Islands, California. *J. geophys. Res.* **90**, 12,485–12,502.

Khair, K., Khawlie, M., Haddad, F., Barazangi, M., Seber, D. & Chaimov, T. 1990. Bouguer gravity and crustal structure of the Dead Sea transform fault and adjacent mountain belts in Lebanon. *Geology* **21**, 739–742.

Lamb, S. H. 1987. A model for tectonic rotations about a vertical axis. *Earth Planet. Sci. Lett.* **84**, 75–86.

Lister, G. S. & Williams, P. F. 1983. The partitioning of deformation in flowing rock masses. *Tectonophysics* **92**, 1–13.

Lovelock, P. E. R. 1984. A review of the tectonics of the northern Middle East region. *Geol. Mag.* **121**, 577–587.

Luyendyk, B. P. 1989. Crustal rotation and fault slip in the continental transform zone in southern California. In: *Paleomagnetic Rotations and Continental Deformation* (edited by Kissel, K. & Laj, C.). Kluwer, Dordrecht, 229–246.

Luyendyk, B. P., Kamerling, M. J. & Terres, R. R. 1980. Geometric model for Neogene crustal rotations in southern California. *Bull. geol. Soc. Am.* **91**, 211–217.

Luyendyk, B. P., Kamerling, M. J., Terres, R. R. & Hornafius, J. S. 1985. Simple shear of southern California during Neogene time suggested by paleomagnetic declinations. *J. geophys. Res.* **90**, 12,454–12,466.

Mann, P., Draper, G. & Burke, K. 1985. Neotectonics of a strike-slip restraining bend system, Jamaica. In: *Strike-Slip Deformation, Basin Formation, and Sedimentation* (edited by Biddle, K. T. & Christie-Blick, N.). *Spec. Publs Soc. econ. Palaeont. Miner.* **37**, 211–226.

Mann, P., Hempton, M. R., Bradley, D. C. & Burke, K. 1983. Development of pull-apart basins. *J. Geol.* **91**, 529–554.

May, S. R., Ehman, K. D., Gray, G. G. & Crowell, J. C. 1993. A new angle on the tectonic evolution of the Ridge basin, a "strike-slip" basin in southern California. *Bull. geol. Soc. Am.* **105**, 1357–1372.

McKenzie, D. P. & Jackson, J. A. 1983. The relationship between strain rates, crustal thickening, palaeomagnetism, finite strain and fault movements within a deforming zone. *Earth Planet. Sci. Lett.* **65**, 182–202. (Correction: **70**, 444, 1984.)

McKenzie, D. P. & Jackson, J. A. 1986. A block model of distributed deformation by faulting. *J. geol. Soc. Lond.* **143**, 349–353.

Michael, E. D. 1966. Large lateral displacement on Garlock fault, California, as measured from offset fault system. *Bull. geol. Soc. Am.* **77**, 111–114.

Muehlberger, W. R. & Gordon, M. B. 1987. Observations on the complexity of the East Anatolian fault, Turkey. *J. Struct. Geol.* **9**, 899–903.

Quennell, A. M. 1958. The structural and geomorphic evolution of the Dead Sea rift. *Q. J. geol. Soc. Lond.* **114**, 1–24.

Ramsay, J. G. 1967. *Folding and Fracturing of Rocks*. McGraw-Hill, New York.

Reches, Z. 1987. Mechanical aspects of pull-apart basins and push-up swells with applications to the Dead Sea transform. *Tectonophysics* **141**, 75–88.

Rockwell, T. K., Keller, E. A., Clark, M. N. & Johnson, D. L. 1984. Chronology and rates of faulting of Ventura River terraces, California. *Bull. geol. Soc. Am.* **95**, 1466–1474.

Rodgers, D. A. 1980. Analysis of pull-apart basin development produced by en échelon strike-slip faults. In: *Sedimentation in Oblique-Slip Mobile Zones* (edited by Ballance, P. F. & Reading, J. G.). *Spec. Publs Int. Ass. Sediment.* **4**, 27–41.

Ron, H. 1987. Deformation along the Yammuneh, the restraining bend of the Dead Sea transform: Paleomagnetic data and kinematic implications. *Tectonics* **6**, 653–666.

Ron, H., Nur, A. & Eyal, Y. 1990. Multiple strike-slip fault sets: a case study from the Dead Sea transform. *Tectonics* **9**, 1421–1432.

Sanderson, D. J. & Marchini, W. R. S. 1984. Transpression. *J. Struct. Geol.* **6**, 449–458.

Sauber, J., Thatcher, W., Solomon, S. S. & Lisowski, M. 1994. Geodetic slip rate for the eastern California shear zone and the recurrence time of Mojave desert earthquakes. *Nature* **367**, 264–266.

Savage, J. C., Prescott, W. H., Lisowski, M. & King, N. E. 1981. Strain accumulation in southern California, 1973–1980. *J. geophys. Res.* **86**, 6991–7001.

Sawal, T., Al-Saad, D., Gebran, A., Barazangi, M., Best, J. A. & Chaimov, T. A. 1993. Stratigraphy and structure of eastern Syria across the Euphrates depression. *Tectonophysics* **220**, 267–281.

Sclater, J. G., Hellinger, S. & Tapscott, C. 1977. The paleobathymetry of the Atlantic Ocean from the Jurassic to the present. *J. Geol.* **85**, 509–552.

Segall, P. & Pollard, D. D. 1980. The mechanics of discontinuous faults. *J. geophys. Res.* **85**, 4337–4350.

Sharp, R. V. 1967. San Jacinto fault zone in the Peninsular Ranges of southern California. *Bull. geol. Soc. Am.* **78**, 705–730.

Sieh, K. E. 1978. Prehistoric large earthquakes produced by slip on the San Andreas fault at Pallett Creek, California. *J. geophys. Res.* **83**, 3907–3939.

Sieh, K. E. 1984. Lateral offsets and revised dates of large prehistoric earthquakes at Pallett Creek, southern California. *J. geophys. Res.* **89**, 7641–7670.

Sieh, K. E. & Jahns, R. J. 1984. Holocene activity on the San Andreas fault at Wallace Creek, California. *Bull. geol. Soc. Am.* **95**, 883–896.

Sieh, K. E., Stuiver, M. & Brillinger, D. 1989. A more precise chronology of earthquakes produced by the San Andreas fault in southern California. *J. geophys. Res.* **94**, 603–623.

Smith, G. I. 1962. Large lateral displacement on Garlock fault, California, as measured from offset dike swarms. *Bull. Am. Ass. Petrol. Geol.* **46**, 85–104.

Sonder, L. J. 1990. Effects of density contrasts on the orientation of stresses in the lithosphere: Relation to principal stress directions in the Transverse Ranges, California. *Tectonics* **9**, 761–771.

Stanley, R. G. 1987. New estimates of displacement along the San Andreas fault in central California based on paleobathymetry and paleogeography. *Geology* **15**, 171–174.

Stock, J. M. & Hodges, K. V. 1989. Pre-Pliocene extension around the Gulf of California and the transfer of Baja California to the Pacific plate. *Tectonics* **8**, 99–115.

Sultan, M., Becker, R., Arvidson, R. E., Shore, P., Stern, R. J., El Alfy, Z. & Attia, R. I. 1993. New constraints on Red Sea rifting from correlations of Arabian and Nubian Neoproterozoic outcrops. *Tectonics* **12**, 1303–1319.

Terres, R. R. & Luyendyk, B. P. 1985. Neogene tectonic rotation of the San Gabriel region, California, suggested by paleomagnetic vectors. *J. geophys. Res.* **90**, 12,467–12,484.

Van Dongen, P. G., Van der Voo, R. & Raven, T. 1967. Paleomagnetism and the Alpine tectonics of Eurasia 3: Paleomagnetic research

in the central Lebanon mountains and in the Tartous area (Syria). *Tectonophysics* **4**, 35–53.
Walley, C. D. 1988. A braided strike-slip model for the northern continuation of the Dead Sea fault and its implications for Levantine tectonics. *Tectonophysics* **145**, 63–72.
Weldon, R. J. & Sieh, K. 1986. Holocene rates of slip and tentative recurrence interval for large earthquakes on the San Andreas fault, Cajon Pass, southern California. *Bull. geol. Soc. Am.* **96**, 793–812.
Wesnousky, S. G. 1986. Earthquakes, Quaternary faults and seismic hazard in California. *J. geophys Res.* **91**, 12,587–12,631.
Westaway, R. 1990. Block rotation in western Turkey 1. Observational evidence. *J. geophys. Res.* **95**, 19,857–19,884.
Westaway, R. 1993. Comment on "velocity fields in deforming Asia from the inversion of earthquake-released strains" by W. E. Holt and A. J. Haines. *Tectonics* **12**, 1485–1488.
Westaway, R. 1994. Present-day kinematics of the Middle East and eastern Mediterranean. *J. geophys. Res.* **99**, 12,071–12,090.
Yeats, R. S. 1983. Large-scale Quaternary detachments in Ventura basin, southern California. *J. geophys. Res.* **88**, 569–583.
Zoback, M. D., Zoback, M. L., Mount, V. S., Suppe, J., Eaton, J. P., Healy, J. H., Oppenheimer, D., Reasenberg, P., Jones, L., Raleigh, C. B., Wong, I. G., Scotti, O. & Wentworth, C. 1987. New evidence on the state of stress of the San Andreas fault system. *Science* **238**, 1105–1111.

APPENDIX A

Analytic solutions for the kinematics of stepovers

Deformation around a stepover is modelled as in Fig. 1. A right-handed (x, y, z) Cartesian coordinate system can be defined with its y-axis parallel to the transform faults, at angle θ to the internal strike-slip fault, and its z-axis vertical. However, the analysis is greatly simplified if a different (u, w, z) coordinate system is used instead, with the u-axis parallel to the internal fault. All angles are measured relative to this axis.

$2U$ and $2V$ are the slip rates on the internal fault and the transform faults, with $k = U/V$. W is the width of the stepover perpendicular to the plate motion. L and H are its length and half-width, parallel and perpendicular to the internal fault. The reference frame used is moving relative to both plates at rate V, such that plates 1 and 2 have $v_y = -V$ and $v_y = +V$. The stepover thus maintains fixed position and orientation relative to the axes and, being symmetrical relative to both plates, only one half need be analysed. The trapezium-shaped deforming zone on each side of the internal fault (Fig. 1a) can be approximated as a rectangle, within which deformation is assumed uniform. If its length $L = W/\sin(\theta)$ is large compared with H, as is usual, this shape adjustment is unimportant.

Deformation at any point in this (u, w) plane is completely described using the horizontal velocity gradient tensor $\mathbf{L}$, where $L_{ij} = \partial v_i/\partial x_j$, $i,j = u,w$. By inspection of Fig. 1, the deformation around a stepover involves components of distributed simple shear parallel to the internal fault (g) and shortening pure shear perpendicular to it (h):

$$L_{uu} = 0 \tag{A1}$$

$$L_{uw} = m[V\cos(\theta) - U]/H = mV[\cos(\theta) - k]/H = g \tag{A2}$$

$$L_{wu} = 0 \tag{A3}$$

$$L_{ww} = -V\sin(\theta)/H = h, \tag{A4}$$

where m is $+1$ or -1 for right- and left-lateral fault zones. Note that h is negative and, with $k < \cos(\theta)$, g is positive for right-lateral slip and *vice* versa. The long faces of each deforming zone coverge in the direction Λ relative to the u-axis, where

$$\tan(\Lambda) = \frac{-mV\sin(\theta)}{V\cos(\theta) - U} = \frac{-m\sin(\theta)}{\cos(\theta) - k} = \frac{h}{g} \tag{A5}$$

at rate v_s where

$$v_s = V(\sin^2(\theta) + [\cos(\theta) - k]^2)^{1/2}. \tag{A6}$$

The deformation is instead more complex when expressed in the (x,y) coordinate system. All four velocity gradient tensor elements are nonzero, making solutions more difficult to obtain. This is the main reason why it is much simpler to use the (u,w) system.

The vertical vorticity χ_z at any locality is obtained from the antisymmetric portion of $\mathbf{L}$. It equals curl($\mathbf{v}$)$_z$, so

$$\chi_z = \frac{\partial v_w}{\partial u} - \frac{\partial v_u}{\partial w} = 0 - g = -g. \tag{A7}$$

A small rigid equidimensional inclusion within a deforming zone will rotate at rate $\chi_z/2$ (e.g. McKenzie & Jackson 1983), and thus rotates through angle v in time t, where

$$v = \frac{-gt}{2}. \tag{A8}$$

The horizontal strain rate tensor $\mathbf{E}$ is the symmetric part of $\mathbf{L}$. It has two eigenvalues E_1 and E_2, the principal horizontal strain rates, with eigenvectors (principal axes of the strain rate tensor) at azimuths $X_{1,2}$. These satisfy (e.g. Westaway 1993)

$$E_{1,2} = h/2 \pm (h/2)[1 + g^2/h^2]^{1/2} = (h/2)[1 \pm \mathrm{cosec}(\Psi)] \tag{A9}$$

$$\tan(X_{1,2}) = 2E_{1,2}/g = \tan(\Psi)[1 \pm \mathrm{cosec}(\Psi)]$$
$$= \tan(\Psi) \pm \sec(\Psi). \tag{A10}$$

Because $|\mathrm{cosec}(\Psi)| > 1$ (except for $\Psi = 90°$), eigenvalue E_1 with azimuth X_1 is always negative (for shortening), and E_2 with aximuth X_2 is always positive (for extension). Note that X_1 does not coincide with the Ψ-direction. It instead bisects the angle between the Ψ-direction and the w-axis, and thus satisfies

$$\Psi = 2X_1 - 90°. \tag{A11}$$

the other eigenvector being perpendicular to this direction. When Ψ is 90°, $g = 0$. The strain rate tensor has a zero eigenvalue E_2 with an eigenvector azimuth $X_2 = 0$ (i.e. parallel to the u-axis and the internal fault), and a shortening strain rate $E_1 = h$ with an eigenvector with $X_1 = 90°$ (parallel to the w-axis). Only in this case are X_1 and Ψ equal.

As noted, e.g. by Westaway (1993) there are in general three possible conditions for the eigenvalues of $\mathbf{E}$: (1) one eigenvalue is zero; (2) both have the same sign; and (3) they have opposite signs. Condition (1) results when $E_{uu}E_{ww} = E_{uw}{}^2$. This occurs when $g = 0$, which means $k = \cos(\theta)$ [equation (A2)], or $\Psi = 90°$. I designate this critical value of k as k_0. The result [equation (A9)], that except for this special case the eigenvalues of the strain rate tensor always have opposite sign, means that case (2) is never satisfied for stepovers: case (3) is always satisfied instead, which means that

$$k < \cos(\theta) \tag{A12}$$

and there are two directions of no length change (Westaway 1993). These satisfy

$$\tan(\phi_{1,2}) = \frac{-E_{uu} \mp [E_{uu}^2 - E_{uu}E_{ww}]^{1/2}}{E_{uw}} = \frac{-g \pm g}{2h} \tag{A13}$$

in general (e.g. Holt & Haines 1993), which means $\tan(\phi_1) = 0$ and $\tan(\phi_2) = -g/h$. These directions are thus parallel to the internal fault and perpendicular to the Ψ-direction.

McKenzie & Jackson (1983) showed that, in general, the finite deformation $\mathbf{F}$ when a given velocity gradient tensor $\mathbf{L}$ (which is uniform spatially and over time) persists for time t is obtained by solving the tensor equation

$$\frac{\mathrm{d}\mathbf{F}}{\mathrm{d}t} = \mathbf{L}\mathbf{F}. \tag{A14}$$

They analysed general deformation with nonzero L_{uw} and L_{ww}, using notation with $-2S = h$ and $W = g$. They showed that for this deformation sense $\mathbf{F}$ satisfies:

$$F_{uu} = 1 \tag{A15}$$

$$F_{uw} = (g/h)(\exp(ht) - 1) \tag{A16}$$

$$F_{wu} = 0 \tag{A17}$$

$$F_{ww} = \exp(ht), \tag{A18}$$

[the corrected form of their equation (11), in my notation]. $\mathbf{F}$ deforms any initial vector $\mathbf{x}_0$, embedded in the distributed deformation, into a new vector $\mathbf{x}$, where $\mathbf{x} = \mathbf{F}\,\mathbf{x}_0$. If $\mathbf{x}_0$ is a unit vector with aximuth α_0 and components (x_{0u}, x_{0w}) or $(\cos(\alpha_0), \sin(\alpha_0))$, and $\mathbf{x}$ has components (x_u, x_w), then $\mathbf{x}$ can be expressed as $(M\cos(\alpha), M\sin(\alpha))$, where M, the modulus of vector $\mathbf{x}$, equals $(x_u{}^2 + x_w{}^2)^{1/2}$, and α is the azimuth of this vector.

McKenzie & Jackson (1983) showed that, for deformation satisfying (A15) to (A18), α_0 and α for any vector are interrelated as

$$\cot(\alpha) = \exp(-ht)\cot(\alpha_0) + (g/h)[1 - \exp(-ht)] \quad \text{(A19)}$$

[their equation (18) expressed in my notation and simplified]. Sanderson & Marchini (1984) also investigated this deformation sense, which they characterized by a finite deformation tensor **D** using parameters that I will call ζ, the shortening factor, and γ, the shear strain. These are defined such that the zone shortens parallel to the u-axis to $1/\zeta$ of its original width, and a vector originally parallel to this axis is deflected through angle Ψ, where $\tan(\Psi) = \gamma$. Their x and y axes are equivalent to my u and w; their α, γ and φ are equivalent to my ζ, γ and α. They showed that **D** satisfies

$$D_{xx} = 1 \quad \text{(A20)}$$

$$D_{xy} = \gamma \quad \text{(A21)}$$

$$D_{yx} = 0 \quad \text{(A22)}$$

$$D_{yy} = 1/\zeta \quad \text{(A23)}$$

[their equation (1) in my notation]. The final orientation of α of a vector with initial orientation α_0 thus satisfies

$$\cot(\alpha) = \zeta\cot(\alpha_0) + \gamma \quad \text{(A24)}$$

In terms of my notation,

$$\zeta = \exp(-ht) \quad \text{(A25)}$$

Substituting $\alpha_0 = 90^\circ$ [$\cot(\alpha_0) = 0$] into (A19) gives $\alpha = 90 - \Psi$, where $\cot(\alpha) = \tan(\Psi) = \gamma$, or

$$\gamma = \frac{g[1 - \exp(-ht)]}{h} = \cot(\Psi)[1 - \zeta] \quad \text{(A26)}$$

Equations (A19) and (A24) are thus consistent. This means that tensors **F** and **D** are equivalent, as is easily verified.

If $\alpha_0 = 0$ ($\cot(\alpha)$ is infinite), then α will remain zero for all time. The rotation ($\alpha - \alpha_0$) of such a vector is zero. If α_0 is nonzero, then from (A19),

$$\frac{\partial\cot(\alpha)}{\partial t} = -h\exp(-ht)\cot(\alpha_0) + g\exp(-ht) \quad \text{(A27)}$$

Thus, $\partial/\partial t[\cot(\alpha)] = 0$ when

$$\tan(\alpha_0) = h/g \quad \text{or} \quad \alpha_0 = \arctan(h/g) - \Psi \quad \text{(A28)}$$

A vector with azimuth Ψ will keep this orientation throughout time. This direction of no rotation is thus identical to Λ (A5), the convergence direction across the deforming zone. Positive h/g requires either extension and right-lateral shear (h and g positive), which cannot occur around a stepover, or shortening and left-lateral shear (h and g negative). With h and g both negative: if $\alpha_0 < \Psi$ then $\partial/\partial t(\cot(\alpha)) < 0$, causing α to decrease, reaching 0° as t tends to infinity; if $\alpha_0 > \Psi$ then $\partial/\partial t(\cot(\alpha)) > 0$, causing α to increase, reaching 180° as t tends to infinity. The orientation $\alpha = 0$ is thus stable; other initial orientations will tend to become deflected towards it; $\alpha = \Psi$ is unstable, as any small perturbation away from it will lead to an ever-increasing deflection. Similar sets of results apply when h negative and g positive. After prolonged shortening and distributed simple shear, paleomagnetic vectors thus become deflected either parallel to or antiparallel to the shear plane; after prolonged extension and distributed simple shear they would instead point parallel to azimuth Ψ. The maximum possible rotation is thus either 180° − Ψ or Ψ, whichever is larger. Where g and h satisfy (A1) to (A4),

$$\tan(\Psi) = \frac{m\sin(\theta)}{\cos(\theta) - k} \quad \text{(A29)}$$

which is equivalent to (A5) with $\Psi = \Lambda$.

For deformation consistent with (A1) to (A4), (A9) can be rearranged, depending on which parameters are unknown. Potentially useful examples include

$$k = \cos(\theta) + \sin(\theta)\frac{m\zeta\cot(\alpha_0) - \cot(\alpha)}{(\zeta - 1)} \quad \text{(A30)}$$

$$\cos(\theta) = m\sin(\theta)\cot(\Psi) + k \quad \text{(A30)}$$

if k is unknown, or

$$\zeta = \frac{\cot(\alpha) - \cot(\Psi)}{\cot(\alpha_0) - \cot(\Psi)} \quad \text{(A31)}$$

to give ζ from α_0 and α. Equation (A30) allows (A6) to simplify to

$$v_y = V\sin(\theta)[1 + \cot^2(\Psi)]^{1/2} = V\sin(\theta)\,\mathrm{cosec}(\Psi) = -hH\,\mathrm{cosec}(\Psi). \quad \text{(A32)}$$

Suppose two rock units in a stepover, with different ages 1 and 2, are subjected to the same phase of later deformation, such that they have the same value of ζ, but where their times of formation are sufficiently different for the plate in which they were originally situated to rotate enough for their palaeomagnetic reference directions (in the absence of effects of the later stepover) to be different. With this condition, α_{01} and α_{02} (i.e. α_0 for ages 1 and 2) will be different; so will α_1 and α_2. The stepover now satisfies two versions of (A31) with the same value of ζ: with $\alpha_0 = \alpha_{01}$ and $\alpha_0 = \alpha_{02}$ and $\alpha = \alpha_1$ and $\alpha = \alpha_2$. One can thus eliminate ζ, and solve for Ψ, the only remaining unknown:

$$\cot(\Psi) = \frac{\cot(\alpha_2)\cot(\alpha_{01}) - \cot(\alpha_1)\cot(\alpha_{02})}{\cot(\alpha_2) + \cot(\alpha_{01}) - \cot(\alpha_1) - \cot(\alpha_{02})}. \quad \text{(A33)}$$

This prediction that the rotation sense of vectors embedded in the deformation around stepovers reverses on either side of two directions ($\alpha = 0$ and $\alpha = \Psi$) can be compared with an alternative prediction, from Lamb (1987), which considers rigid elliptical inclusions. These have elongation (ratio of length of major to minor axes) K, and rotate in a zone of distributed deformation. In this case, the stationary states (where the rotation rate is zero and across which the rotation sense reverses) depend on both Ψ and K [which Lamb (1987) called θ and k]. They are given by

$$\alpha = (1/2)\arccos[C\cos^2(\Psi) \pm \sin(\Psi)\cos(\Psi)(\sec^2(\Psi) - C^2)^{1/2}] \quad \text{(A34)}$$

where

$$C = (1 + K^2)/(1 - K^2). \quad \text{(A35)}$$

No stationary states exist where $C^2 < \sec^2(\theta)$, which is equivalent to

$$K > K_{crit} = \frac{[1 - \cos(\Psi)]^{1/2}}{[1 + \cos(\Psi)]^{1/2}}. \quad \text{(A36)}$$

If $K > K_{crit}$ an inclusion will rotate indefinitely in the same sense.

$C = 1$ means $K = 0$, at the limit of extreme elongation of inclusions. With this condition, (A34) simplifies to

$$\alpha = (1/2)\arccos[\cos^2(\Psi) \pm \sin^2(\Psi)], \quad \text{(A37)}$$

which has solutions $\alpha = 0$ or Ψ. The stationary states (and hence other aspects of rotational behaviour) are thus identical for both an extremely elongated inclusion and for distributed deformation with no inclusions present. Thus the rotation of a highly elongated inclusion (C nearly 1, K just above 0) will be *almost* identical to the rotation within distributed deformation with no inclusions present. This means that any tectonic model incorporating very elongated inclusions can be superceded, to a good approximation, by a model expressed in terms of distributed deformation, which is arguably more realistic. This point appears to have escaped the attention of advocates of models based on rigid inclusions. For instance, the interpretations of rotation observations in the surroundings to the San Andreas fault zone suggested by Lamb (1987) and Jackson & Molnar (1990), which required elongated inclusions, can be replaced as in the main text by a model where only distributed deformation is present.

The deformation around stepovers can also be solved graphically. The method used was developed by Lister & Williams (1983) and others to analyse simpler deformation, and is analogous to the familiar Mohr circle construction (e.g. Ramsay 1967, p. 286). The rotation rate Ω of vectors is plotted against E_3, the strain rate for elongation, as a function of orientation α relative to the u-axis.

The vector orientation with maximum rotation rate Ω is obtained by differentiating (A19):

$$\mathrm{cosec}^2(\alpha)\frac{\partial\alpha}{\partial t} = h\exp(-ht)[\cot(\Psi) - \cot(\alpha_0)] \quad \text{(A38)}$$

and considering the limit of $\partial\alpha/\partial t = \Omega$ at time $t = 0$ when $\alpha = \alpha_0$. From (A38), Ω is thus

$$\Omega = h\sin^2(\alpha)[\cot(\Psi) - \cot(\alpha)]. \quad \text{(A39)}$$

The maximum and minimum of Ω satisfy $d\Omega/d\alpha = 0$. By differentiating (A39) and rearranging using standard formulae for $\cos(2\alpha)$ and $\sin(2\alpha)$, these orientations satisfy

$$\cot(2\alpha) = \cot(\Psi) \quad \text{(A40)}$$

such that $\alpha = \Psi/2$ or $\alpha = \Psi/2 + 90°$. The direction $\alpha = \Psi/2$ thus bisects the directions of no rotation ($\alpha = 0$ and $\alpha = \Psi$); the other is perpendicular to it.

The strain rate for elongation of a unit vector $\mathbf{x}_0$ at azimuth α is obtained by solving the tensor equation $\mathbf{F}\mathbf{x}_0 = \mathbf{x}$, where $\mathbf{x}$ is the vector after deformation. Using (A15) to (A18) for the elements of $\mathbf{F}$, the modulus M of vector $\mathbf{x}$ satisfies

$$M = [\cos^2(\alpha) + \sin^2(\alpha)(1 + \xi^2)/\xi^2 + \sin(2\alpha)(\gamma/\xi)]^{1/2}. \quad \text{(A41)}$$

Using (A25) and (A26) in the limit when $gt \ll 1$,

$$M = [\cos^2(\alpha) + \sin^2(\alpha)(1 + g^2t^2)\exp(2ht) + gt\exp(ht)\sin(2\alpha)]^{1/2}, \quad \text{(A42)}$$

so

$$\frac{\partial M}{\partial t} = \frac{[\sin^2(\alpha)[(1 + g^2t^2)2h\exp(2ht) + 2g^2t\exp(2ht)] + g\exp(ht)\sin(2\alpha)(ht + 1)]^{1/2}}{2[\cos^2(\alpha) + \sin^2(\alpha)(1 + g^2t^2)\exp(2ht) + gt\exp(ht)\sin(2\alpha)]^{1/2}}. \quad \text{(A43)}$$

Thus, at time $t = 0$, when

$$\frac{\partial M}{\partial t} = \sin(\alpha)[h\sin(\alpha) + g\cos(\alpha)] = (h/2)\sin(2\alpha)[\cot(\alpha) + \cot(\Psi)] = E_c, \quad \text{(A44)}$$

$$\frac{\partial E_c}{\partial \alpha} = 2\cos(2\alpha)[\tan(\alpha) + \cot(\Psi)] + \sin(2\alpha)\sec^2(\alpha). \quad \text{(A45)}$$

$|E_c|$ is greatest when $\partial E_c/\partial\alpha = 0$. This condition is equivalent to

$$\tan(2\alpha) = -\cot(\Psi) \quad \text{(A46)}$$

which means $\alpha = \Psi/2 + 45°$ or $\alpha = \Psi/2 + 135°$, the familiar eigenvector azimuths X_1 and X_2.

Lister & Williams (1983) presented plots of (in my notation) Ω against E_c, which form circles. Figure A1 shows the plot for g and h both nonzero, which they did not consider, for $\Psi = 38°$. It is also a circle, with the directions of no length change ($\alpha = 0°$ and $\alpha = \Psi + 90°$) along the Ω-axis and those of no rotation ($\alpha = 0°$ and $\alpha = \Psi$) along the E_c-axis. The azimuths that satisfy (A46) mark maximum and minimum E_c, the familiar eigenvalues E_1 and E_2. The directions of maximum and minimum Ω satisfy (A40), and occur when $E_c = h/2$. The circle thus has diameter $E_1 - E_2$, so from (A9) its radius r is cosec(Ψ)/2. Because the distance OJ in Fig. A1 is 1/2 and the distance OC is r, the angle OCJ is Ψ. The circle can thus be constructed for any other Ψ value: it has diameter cosec(Ψ), and is centred on the line at angle Ψ to the Ω-axis that passes through the origin O at ($E_c = 0$, $\Omega = 0$). This graphical method thus enables the deformation around stepovers to be simply quantified.

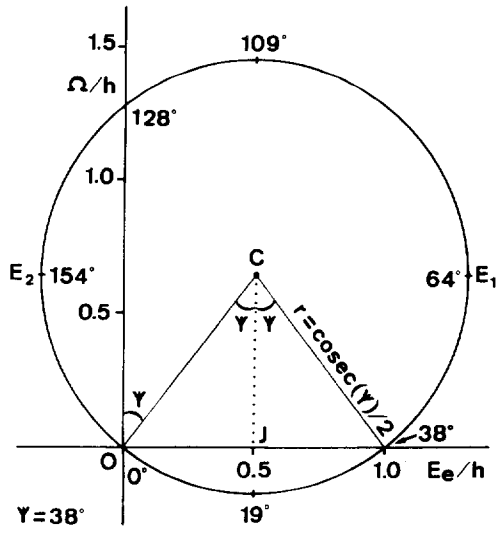

Fig. A1. Graph of Ω/h (normalized rotation rate) against E_c/h (normalized elongational strain rate) for vectors with different azimuths α embedded in the distributed deformation around a stepover, obtained by solving equations (A39) and (A44). For a given value of Ψ the solutions map out a circle, with radius r = cosec(Ψ)/2, which passes through the origin O at ($E_c = 0$, $\Omega = 0$) with centre on a line at angle Ψ to the Ω-axis. The figure is drawn for $\Psi = 38°$, similar to the value deduced for the Lebanon mountains.

The pole to the Mohr diagram as defined by Cutler & Elliott (1983) for this deformation sense, is the Ψ-direction (the convergence direction of the surroundings to the deforming zone), as can be confirmed by inspection. This construction thus provides a straightforward physical meaning for this pole for this particular deformation sense.